

**This item is the archived peer-reviewed author-version of:**

Crystalline tin disulfide by low-temperature plasma-enhanced atomic layer deposition as an electrode material for Li-Ion batteries and CO<sub>2</sub> electroreduction

**Reference:**

Mathew Femi, Van den Hoek Järi, Poonkottil Nithin, Zhao Bo, Rampelberg Geert, Choukroun Daniel, Hereijgers Jonas, Hens Zeger, Poelman Dirk, Breugelmans Tom, ....- Crystalline tin disulfide by low-temperature plasma-enhanced atomic layer deposition as an electrode material for Li-Ion batteries and CO<sub>2</sub> electroreduction

ACS applied energy materials - ISSN 2574-0962 - 6:24(2023), p. 12526-12538

Full text (Publisher's DOI): <https://doi.org/10.1021/ACSAEM.3C02470>

To cite this reference: <https://hdl.handle.net/10067/2013950151162165141>

1  
2  
3  
4  
5  
6  
7  
8  
9  
10  
11  
12  
13  
14  
15  
16  
17  
18  
19  
20  
21  
22  
23  
24  
25  
26  
27  
28  
29  
30  
31  
32  
33  
34  
35  
36  
37  
38  
39  
40  
41  
42  
43  
44  
45  
46  
47  
48  
49  
50  
51  
52  
53  
54  
55  
56  
57  
58  
59  
60

# Crystalline Tin Disulfide by Low-Temperature Plasma-Enhanced Atomic Layer Deposition as Electrode Material for Li-ion Batteries and CO<sub>2</sub> Electroreduction

Femi Mathew,<sup>†</sup> Järi Van den Hoek,<sup>‡</sup> Nithin Poonkottil,<sup>†</sup> Bo Zhao,<sup>†</sup> Geert Rampelberg,<sup>†</sup>  
Daniel Choukroun,<sup>‡</sup> Jonas Hereijgers,<sup>‡</sup> Zeger Hens,<sup>§</sup> Dirk Poelman,<sup>§</sup> Tom Breugelmans,<sup>‡</sup>  
Christophe Detavernier,<sup>†</sup> and Jolien Dendooven<sup>†\*</sup>

<sup>†</sup> Department of Solid State Sciences, COCOON, Ghent University, Krijgslaan 281/S1, B-9000 Ghent, Belgium

<sup>§</sup> Department of Solid State Sciences, LumiLab, Ghent University, Krijgslaan 281/S1, B-9000 Ghent, Belgium

<sup>‡</sup> Applied Electrochemistry & Catalysis (ELCAT), University of Antwerp, Universiteitsplein 1, 2160 Wilrijk, Belgium

<sup>§</sup> Department of Chemistry, Physics and Chemistry of Nanostructures, Ghent University, Krijgslaan 281/S3, B-9000 Ghent, Belgium

\* Corresponding author: [Jolien.Dendooven@UGent.be](mailto:Jolien.Dendooven@UGent.be)

## ABSTRACT

Tin disulfide (SnS<sub>2</sub>) is a promising candidate for electrochemical applications, showcasing improved performance via tailored structure and morphology. This study discusses a plasma-enhanced atomic layer deposition (PE-ALD) method for depositing crystalline SnS<sub>2</sub> thin films using tetrakis(dimethylamino)tin(IV) precursor and H<sub>2</sub>S plasma at a temperature of 80 °C and 180 °C. X-ray diffraction confirms a layered hexagonal crystal structure and strong *c*-axis-

oriented film growth with the alignment of the basal planes mainly parallel to the substrate. At 80 °C, the film surface consists of continuous grain-like structures, whereas, at 180 °C, the smooth film surface during the initial growth evolves to out-of-plane oriented structures when more SnS<sub>2</sub> is deposited. The influence of crystallinity and surface morphology on the electrochemical performance of crystalline SnS<sub>2</sub> thin films deposited by the PE-ALD process is evaluated for lithium-ion battery and electrochemical CO<sub>2</sub> reduction applications. A comparison is made with amorphous SnS<sub>2</sub> thin films deposited by the corresponding thermal ALD process. As an anode material in Li-ion batteries, SnS<sub>2</sub> thin film with out-of-plane oriented structures outperforms the other films with 77% capacity retention after 100 charge/discharge cycles despite its lower initial capacity. In contrast, the crystalline SnS<sub>2</sub> with grain-like morphology and amorphous SnS<sub>2</sub> retain only 65% and 34% respectively of the initial capacity after 100 charge/discharge cycles regardless of their higher initial capacity. In a similar fashion, the SnS<sub>2</sub> thin films with out-of-plane oriented structures exhibit lower Faradaic efficiencies for formate production by CO<sub>2</sub> electroreduction at 100 mA cm<sup>-2</sup> as compared to the SnS<sub>2</sub> with grains (i.e. 64% vs. 80%) albeit at lower overpotentials (i.e. 260 mV less negative) and maintaining a better structural and electrochemical stability. The amorphous SnS<sub>2</sub> thin film showed similar Faradaic efficiencies (i.e. 80%), stability, and overpotentials (i.e. -0.84 V vs RHE) compared to the crystalline SnS<sub>2</sub> thin film with grain-like morphology.

**Keywords** : Plasma-enhanced atomic layer deposition, Tin disulfide, Crystalline thin films, Li-ion battery, CO<sub>2</sub> electroreduction

## 1. INTRODUCTION

In the realm of two-dimensional (2D) materials, transition metal dichalcogenides (TMD's) have attracted significant scientific interest in the past years.<sup>1</sup> This group of TMD's encompasses MoS<sub>2</sub>, WS<sub>2</sub>, and WSe<sub>2</sub>, etc., which appear to be forerunners in the fields of catalysis,<sup>2-3</sup> energy storage and conversion,<sup>4-5</sup> electronics,<sup>6-7</sup> optoelectronics,<sup>8-9</sup> and sensors.<sup>10-12</sup> Like these TMD's, SnS<sub>2</sub> is also a layered metal dichalcogenide (LMD) consisting of covalently bonded in-plane atoms, and successive layers are held together by van der Waals forces.<sup>13</sup> Due to an optical bandgap in the range of 2.1 to 2.4 eV,<sup>14</sup> SnS<sub>2</sub> turns out to be a promising candidate in the domains of photovoltaics<sup>15-16</sup> and photocatalysis.<sup>17-19</sup> Besides, SnS<sub>2</sub> is known for its electrochemical properties with application potential as an anode material in Li-ion batteries, and a catalyst for CO<sub>2</sub> electroreduction.<sup>20-21</sup>

Owing to its high theoretical capacity and lower operating potential over the commercial graphite electrode, SnS<sub>2</sub> finds its place among the most investigated anode materials in Li-ion batteries.<sup>22</sup> This high capacity is attributed to the conversion and alloying reactions occurring during the lithiation/delithiation cycles.<sup>23</sup> Also, being a 2D material with a large interlayer distance (0.59 nm), SnS<sub>2</sub> facilitates the diffusion of lithium ions during charge/discharge cycles.<sup>24</sup>

Moreover, SnS<sub>2</sub> is a potential substitute for pure metal-based catalysts (for example, Pd, Cd, Pb, and Hg) in the electrochemical reduction reaction of CO<sub>2</sub> (CO<sub>2</sub>RR) thanks to its earth-abundant constituents, eco-friendliness, and low cost.<sup>25</sup> In addition, SnS<sub>2</sub> is well known for its selectivity towards formate/formic acid.<sup>26</sup> Among the different CO<sub>2</sub>RR products, formate/formic acid is a liquid fuel product attractive in view of easy storage and transport.

One efficient strategy to further enhance the electrochemical performance of SnS<sub>2</sub> is by modulating crystallinity and morphology.<sup>24, 27</sup> Appropriate control of the morphology and

1  
2  
3 structure of SnS<sub>2</sub> anodes can provide more active sites for hosting lithium ions during  
4 charge/discharge cycles in Li-ion batteries.<sup>20</sup> Similarly, SnS<sub>2</sub> electrocatalysts also benefit from  
5 morphological adjustments that induce new sites for CO<sub>2</sub> activation and thereby improve the  
6 catalytic performance.<sup>28</sup>  
7  
8  
9

10  
11  
12  
13 In view of the aforementioned applications, there is a demand for a scalable technique to  
14 deposit SnS<sub>2</sub> with control over thickness, crystallinity, and morphology at lower temperatures.  
15 Atomic layer deposition (ALD) is a thin film deposition technique to grow uniform and  
16 conformal thin films with excellent thickness control.<sup>29</sup> The self-limiting characteristics  
17 established by the alternate pulsing of well-designed chemical precursors render this vapor  
18 phase technique to meet the above requirements.<sup>30</sup> Tin disulfide thin films have previously  
19 been deposited by plasma-enhanced ALD (PE-ALD) of bis(1-dimethylamino-2-methyl-2-  
20 propoxy)tin(II) [Sn(dmamp)<sub>2</sub>]<sup>31</sup> and H<sub>2</sub>S plasma, and thermal ALD of tetrakis(dimethylamino)  
21 tin(IV) [TDMASn], and tin(IV) acetate [Sn(OAc)<sub>4</sub>]<sup>32</sup> precursors each in combination with H<sub>2</sub>S.  
22  
23  
24  
25  
26  
27  
28  
29  
30  
31  
32  
33  
34 Due to its high vapor pressure, the TDMASn precursor has been employed for many Sn-based  
35 ALD processes.<sup>33-36</sup> Combining TDMASn precursor with H<sub>2</sub>S gas resulted in the growth of  
36 amorphous SnS<sub>2</sub> films below 120 °C, and crystalline SnS<sub>2</sub> films in the range of 140 – 150 °C.<sup>37</sup>  
37  
38  
39  
40  
41  
42 Recently, there has been increasing interest in exploring the PE-ALD technique in the  
43 development of LMD materials.<sup>38-39</sup> Beyond the thermally driven ALD process, the PE-ALD  
44 process puts forward more opportunities for developing thin films at lower temperatures with  
45 control over material properties.<sup>40</sup> This inspired us to attempt a PE-ALD-based approach to  
46 deposit SnS<sub>2</sub> thin films and compare their properties with those of films grown by the  
47 corresponding thermal ALD process.  
48  
49  
50  
51  
52  
53  
54

55  
56  
57 Herein, we introduce a PE-ALD method for depositing crystalline SnS<sub>2</sub> thin films using  
58 TDMASn precursor and H<sub>2</sub>S plasma, at temperatures of 80 °C and 180 °C. Even though PE-  
59  
60

1  
2  
3 ALD of SnS<sub>2</sub> thin films has been attempted before,<sup>31</sup> crystalline SnS<sub>2</sub> thin films using ALD at  
4  
5 temperatures as low as 80 °C have not been reported to the best of our knowledge. First, the  
6  
7 growth characteristics of the PE-ALD process and the corresponding thermal ALD process  
8  
9 were evaluated, and this was followed by a comparative study of the synthesized thin films in  
10  
11 terms of their crystallinity, surface morphology, and chemical composition. Moreover, the  
12  
13 optical properties of the PE-ALD deposited SnS<sub>2</sub> thin films were investigated. Finally, we  
14  
15 employed these SnS<sub>2</sub> thin films as anode material in lithium-ion batteries and electrocatalysts  
16  
17 for CO<sub>2</sub>RR and demonstrated the influence of structure and surface morphology on their  
18  
19 electrochemical performance.  
20  
21  
22  
23  
24  
25  
26  
27

## 28 2. EXPERIMENTAL DETAILS

### 29 2.1 Film Growth

30  
31  
32  
33 Tin sulfide thin films were deposited in a home-built pump-type ALD reactor compatible with  
34  
35 H<sub>2</sub>S based on the recommendations by Dasgupta *et al.*<sup>41</sup> This ALD reactor can be pumped  
36  
37 down to a base pressure of below  $6 \times 10^{-6}$  mbar. The chamber walls were heated to 90 °C. The  
38  
39 depositions were performed on native SiO<sub>2</sub>/Si substrates (for ALD process and thin film  
40  
41 characterization), quartz substrates (for optical property characterization), TiN(40 nm)/SiO<sub>2</sub>(20  
42  
43 nm)/Si substrates (for electrochemical tests as Li-ion battery electrode) and porous carbon gas  
44  
45 diffusion electrodes (for CO<sub>2</sub> electroreduction). The metal-organic precursor  
46  
47 tetrakis(dimethylamino)tin (TDMASn) (99% pure, Strem Chemicals) was stored in a glass  
48  
49 bubbler heated to 45 °C and the precursor line temperature was maintained at 55 °C to avoid  
50  
51 precursor condensation. For the TDMASn precursor, Ar was used as a carrier gas. As a  
52  
53 reactant, either pure H<sub>2</sub>S gas (for thermal ALD experiments) or H<sub>2</sub>S gas mixed with Ar in the  
54  
55 ratio 3:2 (for PE-ALD experiments) was used. For the PE-ALD experiments, H<sub>2</sub>S/Ar plasma  
56  
57  
58  
59  
60

1  
2  
3 was ignited at 200 W employing an inductively coupled plasma source in remote plasma  
4 configuration. During the first half cycle, TDMASn precursor was pulsed into the chamber at  
5  
6  $6 \times 10^{-3}$  mbar for a duration of 25 s for both the PE-ALD and thermal ALD process. Over the  
7  
8 second half cycle, for the PE-ALD process, H<sub>2</sub>S/Ar plasma was introduced to the chamber at  
9  
10  $1 \times 10^{-2}$  mbar pressure for 25 s, whereas for the thermal ALD process, H<sub>2</sub>S gas at  $6 \times 10^{-3}$  mbar  
11  
12 was dosed into the chamber for 25 s. In between the pulses of precursor and reactant, the  
13  
14 reaction chamber was pumped down to the base pressure. For simplicity, the thin films  
15  
16 deposited by the PE-ALD process and thermal ALD process at 80 °C and 180 °C temperature  
17  
18 are mentioned using the abbreviations P80, P180, T80, and T180 respectively and the term H<sub>2</sub>S  
19  
20 plasma is used instead of H<sub>2</sub>S/Ar plasma in the following sections.  
21  
22  
23  
24  
25  
26  
27  
28  
29

## 30 2.2 Analysis Techniques

31  
32 The thickness of the SnS<sub>2</sub> thin films was measured *ex-situ* with X-ray reflectivity (XRR) and  
33  
34 X-ray fluorescence (XRF) techniques. The crystallinity of the SnS<sub>2</sub> thin films was studied  
35  
36 utilizing the X-ray diffraction (XRD) technique. Both XRR and XRD were performed in a  
37  
38 Bruker D8 discover system with copper K $\alpha$  radiation and XRF measurements were carried out  
39  
40 using a Bruker Artax system with a molybdenum X-ray source and XFlash Si drift detector  
41  
42 with an acquisition time of 90 s. The roughness of the SnS<sub>2</sub> thin films deposited by the PE-  
43  
44 ALD process hampered the proper fitting of the XRR patterns. Hence, the thickness of those  
45  
46 films was determined based on calibrated XRF measurements. The calibration curve was  
47  
48 obtained by plotting the thickness of smooth T80 thin films, obtained by XRR fitting, against  
49  
50 the corresponding Sn XRF counts [Figure S1]. The surface morphology of the thin films was  
51  
52 studied using Scanning Electron Microscopy (SEM) on an FEI Quanta 200F instrument. The  
53  
54 Energy Dispersive X-ray spectroscopy (EDS) measurements were also conducted on FEI  
55  
56  
57  
58  
59  
60

1  
2  
3 Quanta 200F instrument at 10 keV utilizing an energy dispersive X-ray analysis silicon-drift  
4 detector from the company EDAX.  
5  
6

7  
8 The chemical composition of the SnS<sub>2</sub> films was investigated using X-ray photoelectron  
9 spectroscopy (XPS) on a Thermo Scientific theta probe system equipped with a monochromatic  
10 Al K $\alpha$  X-ray source (1486.7 eV). Depth profiling of the thin films was done using an EX05  
11 Ar<sup>+</sup> ion gun. All the reported binding energy (BE) values were calibrated using the C1s (285  
12 eV) signal as a reference. All the obtained XPS spectra were analyzed using CasaXPS software.  
13  
14  
15  
16  
17  
18  
19

20 A spectrophotometer (Perkin Elmer Lambda 1050) in the ultraviolet-visible range was used for  
21 studying the optical properties of SnS<sub>2</sub> thin films on quartz substrates and the transmittance  
22 spectra of the films were measured in a wavelength range of 250 - 1100 nm.  
23  
24  
25  
26  
27

28 The hydrophilicity of as-deposited SnS<sub>2</sub> thin films was investigated by the sessile-drop  
29 technique employing a contact-angle analyzer (Kruss, DSA30) with deionized water. The  
30 contact angle images were captured by a charge-coupled device video camera and analyzed  
31 using Drop shape Analysis software. The volume of each deionized water droplet used was  
32 set at 1  $\mu$ L.  
33  
34  
35  
36  
37  
38  
39

40 Electrochemical characterization of the thin films as Li-ion battery anode was carried out using  
41 a home-built potentiostat/galvanostat connected to a three-electrode setup in an argon-filled  
42 glovebox.<sup>42</sup> All thin films for this characterization were deposited on TiN(40 nm)/SiO<sub>2</sub>(20  
43 nm)/Si substrates. Lithium ribbons served as the counter/reference electrode, and 1 M LiClO<sub>4</sub>  
44 in propylene carbonate was used as the electrolyte. The cyclic voltammetry measurements were  
45 performed in the voltage range of 0.1 to 3 V at a scan rate of 1 mV s<sup>-1</sup>.  
46  
47  
48  
49  
50  
51  
52  
53

54 The CO<sub>2</sub>RR chronopotentiometry experiments were carried out in a small-scale flow cell with  
55 an exposed geometric electrode area of 1 cm<sup>2</sup>. Three electrodes were used in this system: (i) a  
56 gas diffusion electrode (Sigracet<sup>®</sup> 39BB, SGL Carbon) with atomic layer deposited SnS<sub>2</sub> as  
57  
58  
59  
60

1  
2  
3 working electrode, (ii) a leak-free 3 M Ag/AgCl electrode (Harvard Apparatus) as reference  
4 electrode, and (iii) a Ni foam (Nanografi Nano Technology) as the counter electrode. CO<sub>2</sub> gas  
5 was fed to the reactor using a Brooks flow controller (GF040, 100 sccm) at 25 sccm. The  
6 catholyte and anolyte respectively consisted of a 0.5 M KHCO<sub>3</sub> solution (Chem-Lab, 99.5+%)  
7 (pH 8.6) and a 2 M KOH solution (Chem-Lab, 85+%) which were pumped to the reactor at a  
8 flow rate of 2.6 mL min<sup>-1</sup> using a peristaltic pump (Ismatec ISM4408). These electrolytes were  
9 separated in the reactor by a Nafion 117 cation exchange membrane (CEM). Subsequently, the  
10 catholyte and the CO<sub>2</sub> flow leaving the reactor were separated in a gas-liquid divider with the  
11 gaseous stream consisting of CO<sub>2</sub> and products, such as H<sub>2</sub> and CO, being fed to an in-line gas  
12 chromatograph with a TCD (GC) (Shimadzu 2014 series with a micropacked column (Restek  
13 Shincarbon ST, 2 m, 1 mm ID, 100/120 mesh). The catholyte was pumped from the gas-liquid  
14 divider and sampled every 20 minutes for two minutes to complement the GC analysis. These  
15 liquid samples were analyzed using a high-performance liquid chromatograph (Waters  
16 Alliance HPLC, equipped with a Shodex KC-811 column and a PDA detector (Waters 2996))  
17 to quantify the amount of formate produced. The electrochemical measurement procedure  
18 consisted of electrochemical impedance spectroscopy, chronopotentiometry, and cyclic  
19 voltammetry using a multi Autolab M204 with a FRA module. The latter method was used to  
20 estimate the electrochemical double-layer capacitance ( $C_{dl}$ ) of the various thin films by cycling  
21 from 50 mV s<sup>-1</sup> to 200 mV s<sup>-1</sup> in the non-Faradaic region. Subsequently, the electrochemical  
22 active surface area (EASA) was calculated using the specific capacitance ( $C_s$ ) value of 40 μF  
23 cm<sup>-2</sup> for a flat standard with a geometric area of 1 cm<sup>2</sup> resulting in the following formula:  
24  
25  
26  
27  
28  
29  
30  
31  
32  
33  
34  
35  
36  
37  
38  
39  
40  
41  
42  
43  
44  
45  
46  
47  
48  
49  
50

$$EASA = \frac{C_{dl}}{40 \mu F cm^{-2}} cm_{EASA}^2$$

51  
52  
53  
54  
55  
56  
57 Chronopotentiometry was used to determine the selectivity, activity, and stability of the  
58 catalysts and was used with a current density of 100 mA cm<sup>-2</sup> for six hours. The selectivity was  
59  
60

1  
2  
3 calculated by taking into account the outgoing CO<sub>2</sub> flow rate. All measurements were  
4 replicated two times and average values plus standard deviation are given in the graphs.  
5  
6 Electrochemical impedance spectroscopy was used to derive the uncompensated ohmic  
7 resistance (R<sub>u</sub>) of the catholyte and correct the potential (vs. Ag/AgCl) obtained during the  
8 chronopotentiometry measurement. Conversion to the RHE scale was calculated using the  
9 following formula:

$$E_{RHE} = E_{ref} + 0.059 pH + E_{Ag/AgCl}^{\circ} + iR_u$$

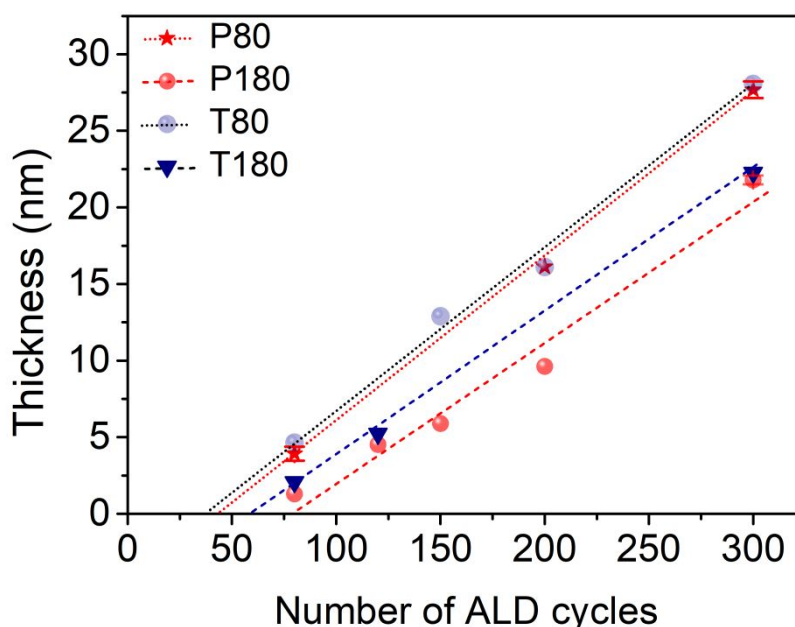
16  
17  
18  
19  
20  
21  
22 Where E<sub>RHE</sub> and E<sub>ref</sub> are the potentials versus the RHE and reference electrode (Ag/AgCl),  
23 respectively. E<sub>Ag/AgCl</sub><sup>°</sup> is the standard electrode potential of the Ag/AgCl system.  
24  
25  
26  
27  
28  
29

### 30 3. RESULTS AND DISCUSSION

#### 31 3.1 ALD Characterization

32  
33 We studied the film growth as a function of the number of ALD cycles for both the PE-ALD  
34 and the thermal ALD process at a low temperature of 80 °C and a high temperature of 180 °C.  
35  
36 Here, one cycle of the ALD process is defined as [T 25 s – P 90 s – H 25 s – P 100 s], where T  
37 and H stand for TDMASn and H<sub>2</sub>S gas or H<sub>2</sub>S plasma, respectively. In between the pulses of  
38 precursor and reactant, the reactor was pumped down to the base pressure which required  
39 pumping times (P) of 90 s and 100 s after TDMASn and H<sub>2</sub>S gas or H<sub>2</sub>S plasma, respectively.  
40  
41 **Figure 1** shows the film thickness after different numbers of ALD cycles in the range of 80 up  
42 to 300 ALD cycles. The film thickness was either determined by XRR, for smooth films, or by  
43 XRF, for the rougher films, as explained in the experimental section. Linear fits to the data  
44 points are included in **Figure 1**. For all investigated processes, the x-intercept of the fitted lines  
45 is observed at several tens of ALD cycles (> 30 cycles), indicative of inhibited growth at the  
46  
47  
48  
49  
50  
51  
52  
53  
54  
55  
56  
57  
58  
59  
60

1  
2  
3 start of the deposition processes. After this incubation period, steady growth behavior is  
4  
5 observed for all processes. While the thermal and PE-ALD processes behave very similarly,  
6  
7 the deposition temperature has an impact on the growth per cycle (GPC) and incubation, with  
8  
9 the highest GPC and lowest incubation observed for the low deposition temperature of 80 °C.  
10  
11 For the thermal ALD process, GPCs of 1.06 Å and 0.92 Å are extracted from the linear fits at  
12  
13 80 °C and 180 °C, respectively. In the previous report by Ham *et al.* on the thermal ALD  
14  
15 process, a slightly higher GPC of 1.31 Å at 80 °C and a slightly lower GPC of 0.35 Å at 180  
16  
17 °C was observed wherein a flow-type reactor was used.<sup>37</sup> Yet, the linearity of the process was  
18  
19 not investigated. The PE-ALD process also demonstrates a linear relationship between  
20  
21 thickness and the number of cycles after the incubation period with a GPC of 1.07 Å at 80 °C  
22  
23 and a GPC of 0.90 Å at 180 °C. The lower GPC obtained in both cases at 180 °C can be  
24  
25 attributed to the decrease in density of surface thiol species at higher temperatures.<sup>43</sup>  
26  
27  
28  
29  
30  
31  
32  
33  
34



1  
2  
3 **Figure 1.** Thickness against the number of ALD cycles for the PE-ALD process and the thermal  
4 ALD process at 80 °C and 180 °C. Some data points represent the average thickness value of  
5 two different samples. Error bars indicate the standard deviation.  
6  
7  
8  
9

10  
11 The self-limiting characteristics of the PE-ALD process were verified by varying the pulse time  
12 of the TDMASn precursor and H<sub>2</sub>S plasma steps at 80 °C. In this series of depositions, 80 ALD  
13 cycles were performed and the exposure time of one reactant was varied, while the other  
14 exposure time was kept constant at 25 s for both thermal ALD and PE-ALD processes. From  
15 the data in **Figure 2**, it can be seen that saturation is observed for both the TDMASn precursor  
16 and H<sub>2</sub>S plasma step. Because the ALD growth is affected by inhibited growth during the first  
17 several tens of ALD cycles, the calculated GPC (0.45 Å) for the 80 cycles depositions is lower  
18 than the GPC that we extracted from the linear fits in **Figure 1** (1.07 Å). Similarly, the  
19 saturation behavior of the PE-ALD process at 180 °C and the thermal ALD processes at 80 °C  
20 and 180 °C was also investigated, suggesting self-limiting reactions for all investigated process  
21 conditions [**Figure S2**]. The TDMASn-H<sub>2</sub>S atomic layer deposition process is anticipated to  
22 follow a ligand exchange mechanism, similar to the gallium sulfide ALD process based on  
23 alkyl amide precursor and H<sub>2</sub>S.<sup>44</sup> Moreover, the surface thiol (-SH) species is expected to play  
24 a similar role as (-OH) species in the oxide ALD processes based on TDMASn precursor and  
25 H<sub>2</sub>O reactant which have also been observed to undergo ligand exchange reaction.<sup>45-46</sup>  
26  
27  
28  
29  
30  
31  
32  
33  
34  
35  
36  
37  
38  
39  
40  
41  
42  
43  
44  
45  
46  
47  
48  
49  
50  
51  
52  
53  
54  
55  
56  
57  
58  
59  
60

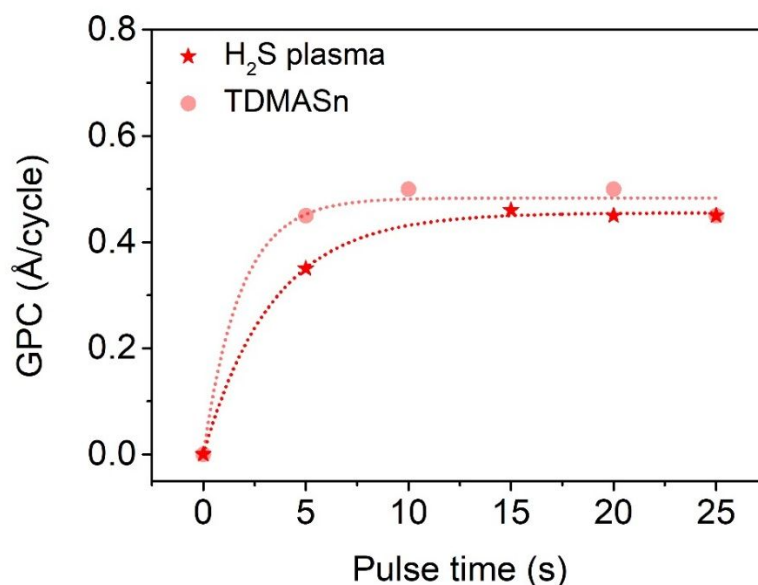


**Figure 2.** GPC against the pulse time of TDMASn and H<sub>2</sub>S plasma for the PE-ALD at 80°C. When the TDMASn (H<sub>2</sub>S plasma) pulse time was varied, the H<sub>2</sub>S plasma (TDMASn) pulse time was fixed at 25 s. Each data point was obtained from 80 ALD cycle depositions, and the GPC was calculated by dividing the obtained thickness by 80. The dotted lines are given as a guide to the eye.

### 3.2 Structural Characterization

The effect of growth temperature on the crystallinity and surface morphology of the thin films deposited by both the PE-ALD process and the thermal ALD process was studied using XRD and SEM, respectively. **Figure 3(a)** shows the XRD pattern of as-deposited films at 80 °C and 180 °C. The XRD pattern of the P80 thin film (28 nm) shows a strong peak around  $2\theta = 14.9^\circ$ , corresponding to the (001) peak of the hexagonal SnS<sub>2</sub> crystal structure along with two weak peaks at  $29.8^\circ$  and  $45.7^\circ$  corresponding to the (002) and (003) crystal planes indicating an orientation effect (JCPDS 23-0677). This means that most of the basal planes of SnS<sub>2</sub> are aligned parallel to the substrate. Similar to the P80 film, the P180 film (21 nm) also shows a

1  
2  
3 peak at  $14.9^\circ$ , revealing a hexagonal  $\text{SnS}_2$  crystal structure. However, the less intense (001)  
4 peak and absence of (002) and (003) peaks for the P180 film suggest a change in basal plane  
5 texture. This is studied in more detail by XRD rocking curve measurements at the (001)  
6 reflection [Figure 3(b)]. A full width at half maximum (FWHM) of  $4.8^\circ$  and  $5.8^\circ$  is obtained  
7 for  $\text{SnS}_2$  films deposited by the P80 and P180 process, respectively. The smaller FWHM for  
8 the P80 film shows the better alignment of basal planes parallel to the substrate in comparison  
9 to the P180 film. Coming back to the thermal ALD process, amorphous thin films are grown  
10 with the T80 process (28 nm), while thin films deposited by the T180 process (22 nm) are  
11 poorly crystalline showing both SnS and  $\text{SnS}_2$  phases with a small XRD peak at  $31.5^\circ$   
12 corresponding to the (111) diffraction of the orthorhombic SnS crystal structure (JCPDS 39-  
13 0354), and a small peak at  $14.9^\circ$  corresponding to the (001) diffraction of the hexagonal  $\text{SnS}_2$   
14 structure. The XRD pattern of the T80 and T180 films in high resolution is added to the  
15 supporting information.[Figure S3] These results are in line with the work by Ham *et al.*<sup>37</sup>  
16 Therefore, compared to the thermal ALD process, the PE-ALD process deposits films with  
17 high crystallinity and preferred orientation at temperatures as low as  $80^\circ\text{C}$ .  
18  
19  
20  
21  
22  
23  
24  
25  
26  
27  
28  
29  
30  
31  
32  
33  
34  
35  
36  
37  
38  
39  
40  
41  
42  
43  
44  
45  
46  
47  
48  
49  
50  
51  
52  
53  
54  
55  
56  
57  
58  
59  
60

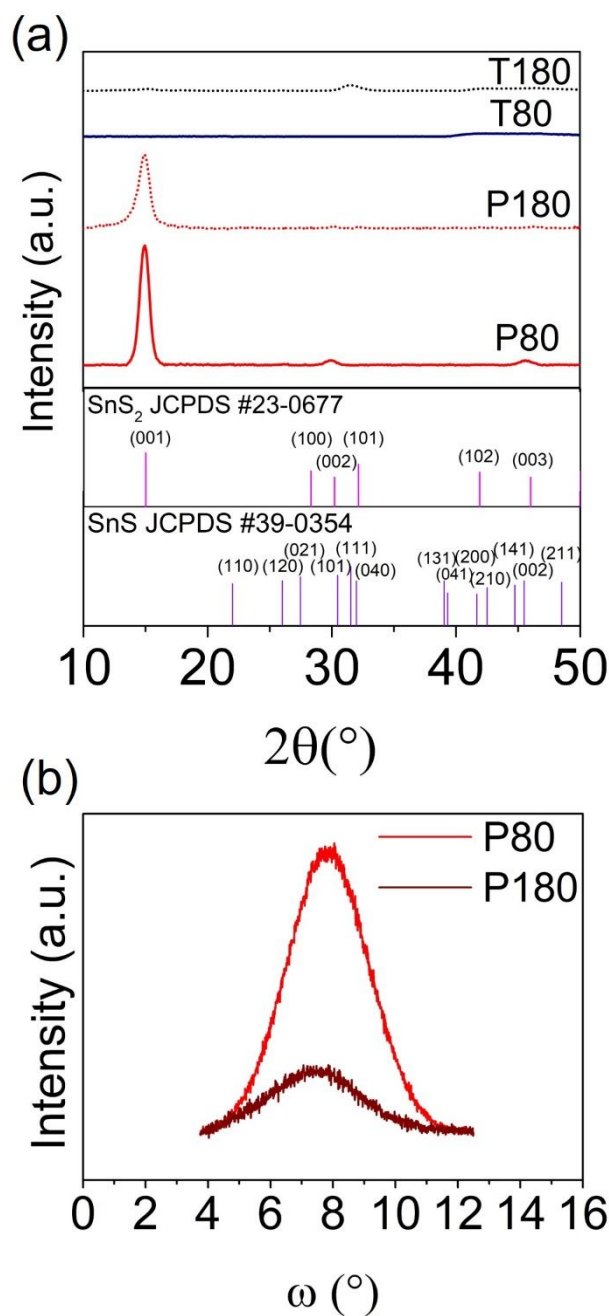


**Figure 3.** (a) XRD patterns of the  $\text{SnS}_x$  films deposited by the PE-ALD and thermal ALD processes at 80  $^{\circ}\text{C}$  and 180  $^{\circ}\text{C}$ . (b) XRD rocking curve measurements for the (001) reflection of  $\text{SnS}_2$  deposited by PE-ALD at 80 $^{\circ}\text{C}$  and 180  $^{\circ}\text{C}$ .

The influence of deposition temperature on the surface morphology of the thin films is evaluated by top-view SEM imaging as shown in **Figure 4**. For the thermal ALD process, smooth thin films are deposited at 80  $^{\circ}\text{C}$ , whereas, at 180  $^{\circ}\text{C}$ , small crystallites are observed,

1  
2  
3 in agreement with the report by Ham *et al.*<sup>37</sup> In contrast, SEM images of PE-ALD films  
4 correspond to rough films. The surface morphology of P80 thin films displays large crystallites  
5 with sizes in the range of 30-50 nm for a film of similar thickness (~22-28 nm), whereas the  
6 P180 films develop out-of-plane oriented (OoPO) structures. Similar behavior of out-of-plane  
7 oriented growth was previously reported for MoS<sub>2</sub> and TiS<sub>2</sub> thin films deposited by PE-ALD.<sup>38</sup>  
8  
9  
10  
11  
12  
13  
14  
15  
16  
17  
18  
19  
20  
21  
22  
23  
24  
25  
26  
27  
28  
29  
30  
31  
32  
33  
34  
35  
36  
37  
38  
39  
40  
41  
42  
43  
44  
45  
46  
47  
48  
49  
50  
51  
52  
53  
54  
55  
56  
57  
58  
59  
60

<sup>47</sup> Surface imaging was done after 80, 150, 200, and 300 ALD cycles of the P180 films corresponding to equivalent film thicknesses of 2, 6, 10, and 21 nm, respectively. **Figure 4(e)** - (h) shows a clear evolution of the surface morphology from an almost smooth surface with discrete crystallites to a film surface dominated by out-of-plane oriented structures. This is in line with the nucleation mechanism put forward by Sharma *et al.* in their study on PE-ALD of MoS<sub>2</sub>.<sup>47</sup> They observed the formation of discrete islands at the beginning of film growth, which coalesced at certain points during subsequent ALD cycles, thus forming a nearly continuous film. In subsequent ALD cycles, film growth occurs at the edges of the islands leading to out-of-plane growth. Here, 80 ALD cycles already show the transition from in-plane to out-of-plane orientation, and out-of-plane oriented mode is clearly visible at 300 ALD cycles.

Additionally, the larger roughness of the PE-ALD films is evident from the X-ray reflectivity (XRR) patterns as shown in **Figure 4(d)**. The XRR pattern of thermal-ALD films displays characteristic fringes, without the significant decrease in intensity and oscillation, suggestive of smooth films. Compared to the smooth films deposited by the thermal ALD process, the XRR intensity of the films deposited by the PE-ALD process decays promptly. Also, among the PE-ALD films, the reflectivity of the films deposited at 180 °C decreases more quickly suggesting higher roughness, consistent with the SEM results.

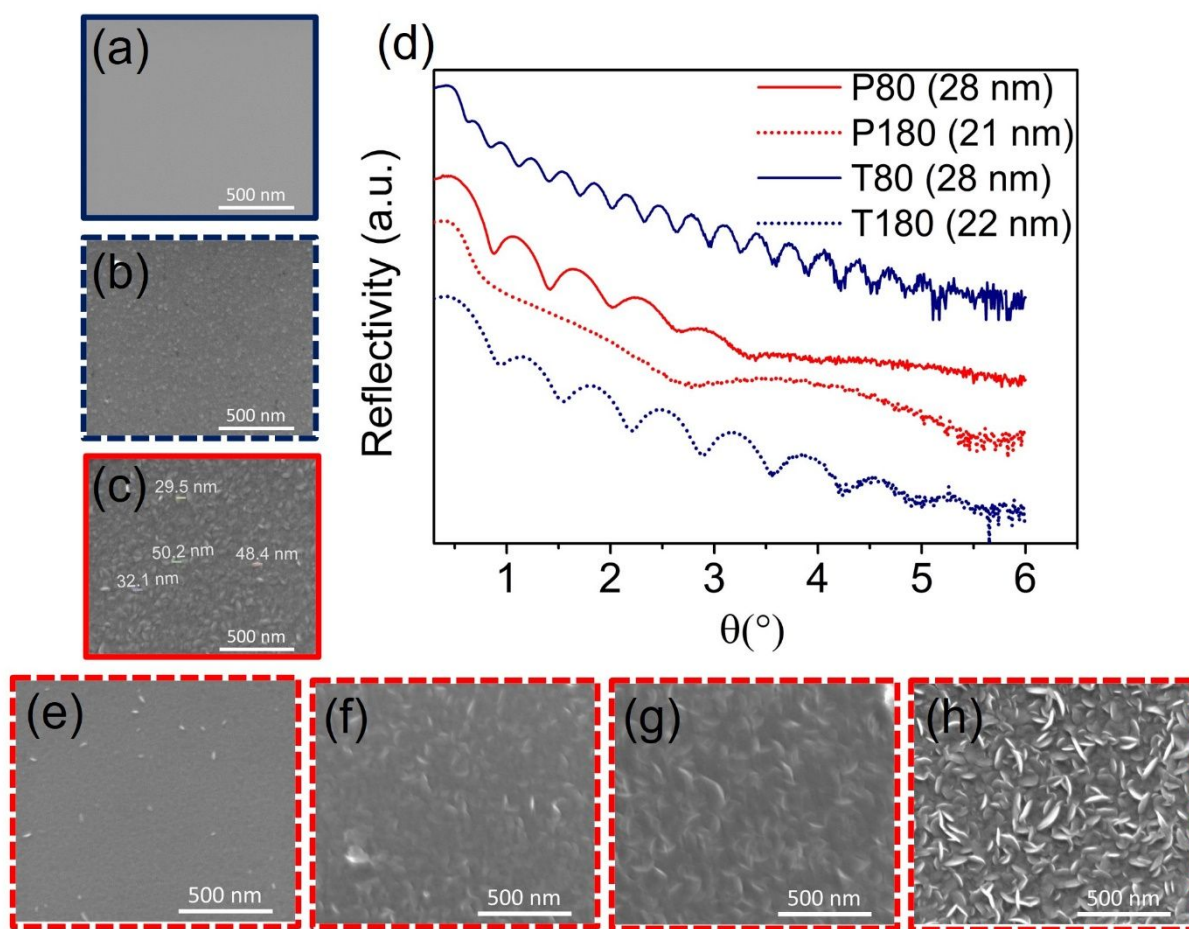


**Figure 4.** Top-view SEM images of films (a) T80 (28 nm) (b) T180 (22 nm) (c) P80 (28 nm) (d) XRR pattern corresponding to the  $\text{SnS}_x$  films and top-view SEM images of P180 films for different ALD cycles (e) P180 (2 nm) (f) P180 (6 nm) (g) P180 (10 nm) (h) P180 (21 nm)

XPS was utilized to investigate the chemical states of tin and sulfur present in the as-deposited thin films. The high-resolution spectra of the S 2p and Sn 3d regions (measured at 50 eV pass energy) were subjected to the Gaussian Lorentzian product function fitting (70% Gaussian character) following Shirley background subtraction as depicted in **Figure 5**. Notably, the Sn  $3d_{5/2}$  spectra of P80 and P180 films are fitted by a single peak at 486.6 and 486.7 eV respectively, attributed to the tetravalent Sn oxidation state.<sup>48-49</sup> Also, the S 2p doublet was deconvoluted into two peaks spaced 1.2 eV apart and with an area ratio of 2:1. These peaks obtained at 161.6 and 162.8 eV correspond to S  $2p_{3/2}$  and S  $2p_{1/2}$  features respectively.

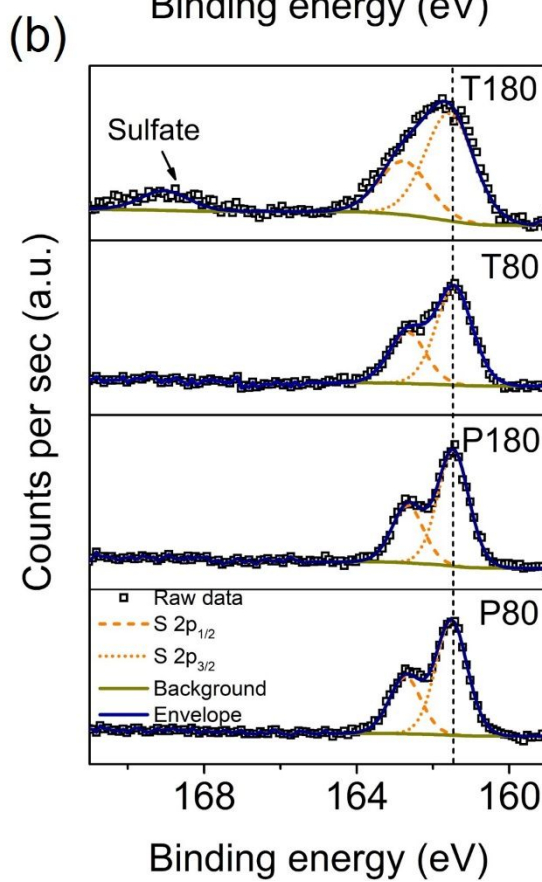
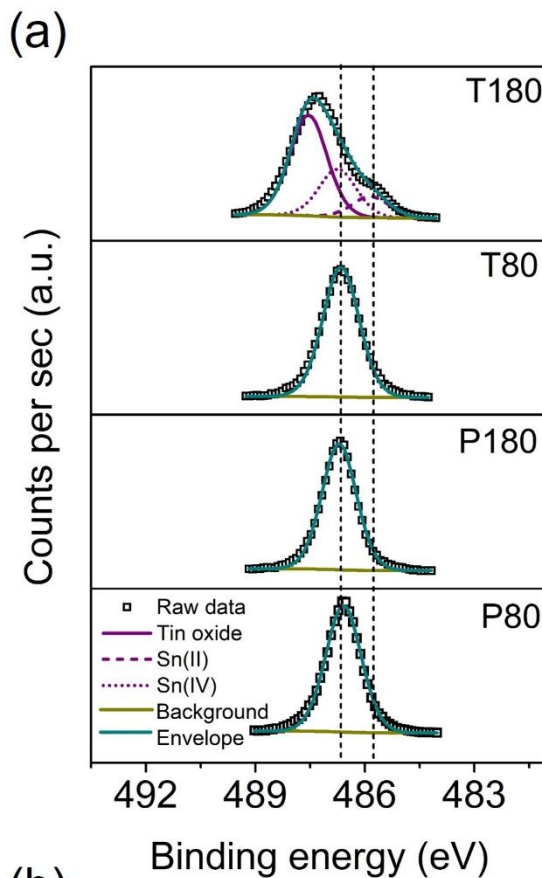
1  
2  
3 Similarly, the T80 film also exhibits a single Sn 3d<sub>5/2</sub> fitted peak alongside a doublet resolved  
4  
5 S 2p peak. The binding energies for Sn 3d<sub>5/2</sub> and S 2p<sub>3/2</sub> peak are at 486.6 eV and 161.6 eV  
6  
7 respectively, thus confirming the SnS<sub>2</sub> phase. In contrast, for the T180 thin film, the Sn 3d<sub>5/2</sub>  
8  
9 spectrum is fitted by three peaks corresponding to the tetravalent and divalent tin with a  
10  
11 separation of 0.9 eV at binding energies of 486.7 and 485.8 eV respectively, with another peak  
12  
13 at 487.5 showing the presence of SnO<sub>2</sub>. In the T180 film, the presence of SnO<sub>2</sub> unlike others  
14  
15 can be attributed to aging as the time gap between sample preparation and measurement was  
16  
17 longer for the T180 film compared to the rest. The obtained S 2p peak is deconvoluted into  
18  
19 doublet peaks at 161.5 and 162.7 eV corresponding to the S 2p<sub>3/2</sub> and S 2p<sub>1/2</sub> features. In  
20  
21 addition, a small feature is observed at 169 eV corresponding to sulfates.<sup>50</sup> It was expected to  
22  
23 see two doublets in the S 2p spectrum of the T180 film, but the deconvolution was challenging  
24  
25 due to the proximity of the S 2p<sub>3/2</sub> binding energies for the SnS and SnS<sub>2</sub> phases and the  
26  
27 resolution constraints of the measured spectrum. However, the higher FWHM of the S 2p<sub>3/2</sub>  
28  
29 spectrum of the T180 compared to the rest of the films (1.5 vs 1.1) suggests the presence of  
30  
31 more than one doublet within the S 2p spectrum. The Sn 3d<sub>5/2</sub> and S 2p<sub>3/2</sub> binding energies of  
32  
33 all as-deposited films are shown in **Table 1** and are in alignment with literature values. These  
34  
35 results are thus in agreement with the crystalline phases observed in the XRD patterns.  
36  
37  
38  
39  
40  
41  
42

43 In addition, the XPS survey scans measured at 200 eV pass energy at the film surfaces and in  
44  
45 the bulk, are shown in **Figure S4**. The film surfaces displayed noticeable contamination arising  
46  
47 from adventitious carbon, nitrogen, and oxygen impurities. Notably, no impurities were  
48  
49 detected in the bulk of the P80, P180, and T80 films. In contrast, for the T180 film, carbon (ca.  
50  
51 5%) and oxygen (ca. 20%) contamination has been observed in the bulk. Table S1 depicts the  
52  
53 atomic concentrations of the detected elements exclusively from the film surfaces, as binding  
54  
55 energy shifts and preferential sputtering of sulfur atoms are observed due to argon sputtering.  
56  
57 For the T180 film, the S/Sn ratio has been calculated by quantifying the Sn 3d component  
58  
59  
60

associated with the Sn-S bonding and the S 2p peaks in the survey scan (measured at 200 eV pass energy) after accounting for Shirley background subtraction and atomic sensitivity factors and is found to be 1.1. In contrast, for the P80, P180, and T80 films, the S/Sn ratios were found to be 1.9, 2.1, and 1.8, respectively, which are closely aligned with SnS<sub>2</sub> stoichiometry.

**Table 1.** XPS binding energies (in eV) of Sn 3d<sub>5/2</sub> and S 2p<sub>3/2</sub> peaks of as-deposited SnS<sub>x</sub> thin films. The FWHM of the fitted peaks are shown in parentheses. Please note that the binding energies reported in this work are subject to an error bar of ±0.2 eV.

Method	Binding energy (eV)		
	Sn 3d <sub>5/2</sub>		S 2p <sub>3/2</sub>
	Sn (IV)	Sn (II)	
PE - ALD process at 80 °C	486.6 (1.0)	-	161.5 (1.0)
PE - ALD process at 180 °C	486.7 (1.1)	-	161.6 (1.0)
Thermal ALD at 80 °C	486.6 (1.1)	-	161.6 (1.1)
Thermal ALD at 180 °C	486.7 (1.1)	485.8 (1.1)	161.5 (1.5)



1  
2  
3 **Figure 5.** (a) & (b) Sn 3d<sub>5/2</sub> and S 2p XPS spectra of SnS<sub>x</sub> thin films deposited by the PE-ALD  
4 and thermal ALD process at 80°C and 180 °C.  
5  
6  
7

8 SnS<sub>2</sub> thin films deposited by the PE-ALD process were investigated for their optical properties  
9 to further complement the analysis of their film quality. SnS<sub>2</sub> thin films were deposited on a  
10 quartz substrate and transmittance measurements were acquired in the wavelength range of 250  
11 to 1100 nm. **Figure S5(a)** shows the transmittance spectra of SnS<sub>2</sub> thin films deposited by the  
12 PE-ALD process at 80 °C and 180 °C with a thickness of 97 nm and 83 nm, respectively. The  
13 spectra are corrected for the transmittance of the bare quartz substrate. Also, the bandgap of  
14 the SnS<sub>2</sub> thin films is obtained from the tauc plot –  $(\alpha h\nu)^{1/2}$  against  $h\nu$  – by extrapolation of a  
15 linear fit to the absorption edge to intersect the  $h\nu$  axis [**Figure S5(b)**]. An indirect bandgap of  
16 2.30 eV and 2.25 eV is obtained for the P80 and P180 thin films respectively, in agreement  
17 with literature values.<sup>51-52</sup>  
18  
19  
20  
21  
22  
23  
24  
25  
26  
27  
28  
29  
30  
31

### 32 **3.3 SnS<sub>2</sub> as anode material for Lithium-ion batteries**

33  
34 The layered structure of SnS<sub>2</sub> makes itself an ideal electrode material for lithium-ion batteries.  
35 SnS<sub>2</sub> has a large interlayer spacing of 0.59 nm, thus facilitating the insertion and extraction of  
36 Li<sup>+</sup> ions.<sup>53</sup> It is known that the SnS<sub>2</sub> material is characterized by insertion, conversion, and  
37 alloying reactions while undergoing the lithiation cycle,<sup>22, 54</sup> Herein, we compare the  
38 electrochemical performance of SnS<sub>2</sub> anode materials deposited by the PE-ALD and thermal  
39 ALD process in the Li-ion battery. For the electrochemical testing, SnS<sub>2</sub> films (~30-40 nm  
40 thickness) deposited on TiN(40 nm)/SiO<sub>2</sub>(20 nm)/Si substrates were used as the anode material.  
41 The SEM images and high-resolution XPS spectra of the Sn 3d and S 2p regions of the SnS<sub>2</sub>  
42 films deposited on TiN substrates by the PE-ALD and thermal ALD process are consistent with  
43 those obtained on the silicon substrates indicating that the film growth is similar on both  
44 substrates [**Figure S6 & S7**]. In addition, the obtained binding energies of the Sn 3d<sub>5/2</sub> and S  
45  
46  
47  
48  
49  
50  
51  
52  
53  
54  
55  
56  
57  
58  
59  
60

1  
2  
3  
4  
5  
6  
7  
8  
9  
10  
11  
12  
13  
14  
15  
16  
17  
18  
19  
20  
21  
22  
23  
24  
25  
26  
27  
28  
29  
30  
31  
32  
33  
34  
35  
36  
37  
38  
39  
40  
41  
42  
43  
44  
45  
46  
47  
48  
49  
50  
51  
52  
53  
54  
55  
56  
57  
58  
59  
60

$2p_{3/2}$  spectra of the as-deposited SnS<sub>2</sub> films, as well as the S/Sn atomic ratio are summarized in **Table S2**.

**Figure 6(a)-(c)** shows the first three cycles of the cyclic voltammetry (CV) profile of P80, P180, and T80 SnS<sub>2</sub> electrodes where the voltage is varied in the range of 0.1 to 3.0 V at a scan rate of 1 mV s<sup>-1</sup>. Both the P80 and P180 films possess similar CV characteristics and redox peak couples for the initial three cycles. The oxidation/reduction reactions occurring during the electrochemical testing of SnS<sub>2</sub> anode material are shown in five steps as in **Figure 7**. In their first lithiation cycle (discharge cycle), two cathodic peaks at 1.8 V and 1.5 V correspond to the multistep insertion of lithium ions into SnS<sub>2</sub> forming Li<sub>x</sub>SnS<sub>2</sub><sup>53</sup> (Step 1). The strong cathodic peak at 1.2 V can be ascribed to the decomposition of Li<sub>x</sub>SnS<sub>2</sub> to Li<sub>2</sub>S and metallic tin as well as the formation of a solid electrolyte interface (SEI)<sup>55-56</sup> (Step 2). This formation of SEI film accounts for the high irreversible capacity of the first charge/discharge cycle.

The redox peak couple formed by the cathodic peak at 0.2 V and anodic peak at 0.4 V can be assigned to the reversible alloying and dealloying of Li<sub>x</sub>Sn (Steps 3 & 4). The set of anodic peaks in the potential range of 1.6 – 1.8 V corresponds to the deconversion back to an altered SnS<sub>x</sub> phase.<sup>54</sup> Also, the peak at 2.3 V corresponds to the conversion of unreacted Li<sub>2</sub>S to polysulfides.<sup>57</sup> In the subsequent cycles, the peaks at 1.8 V and 1.5 V related to the insertion of lithium ions in the SnS<sub>2</sub> layered structure in the subsequent cycles are absent indicating that the SnS<sub>2</sub> crystal structure is not completely restored after the first charge/discharge cycle. However, the constant cathodic peaks at 1.2 V, 0.2 V and anodic peaks at 0.4 V and 1.6 – 2.3 V during the subsequent charge/discharge cycles demonstrate reversible conversion and alloying reactions occurring around the altered SnS<sub>x</sub> phase and are visualized by the reactions shown in the red box in **Figure 7**.

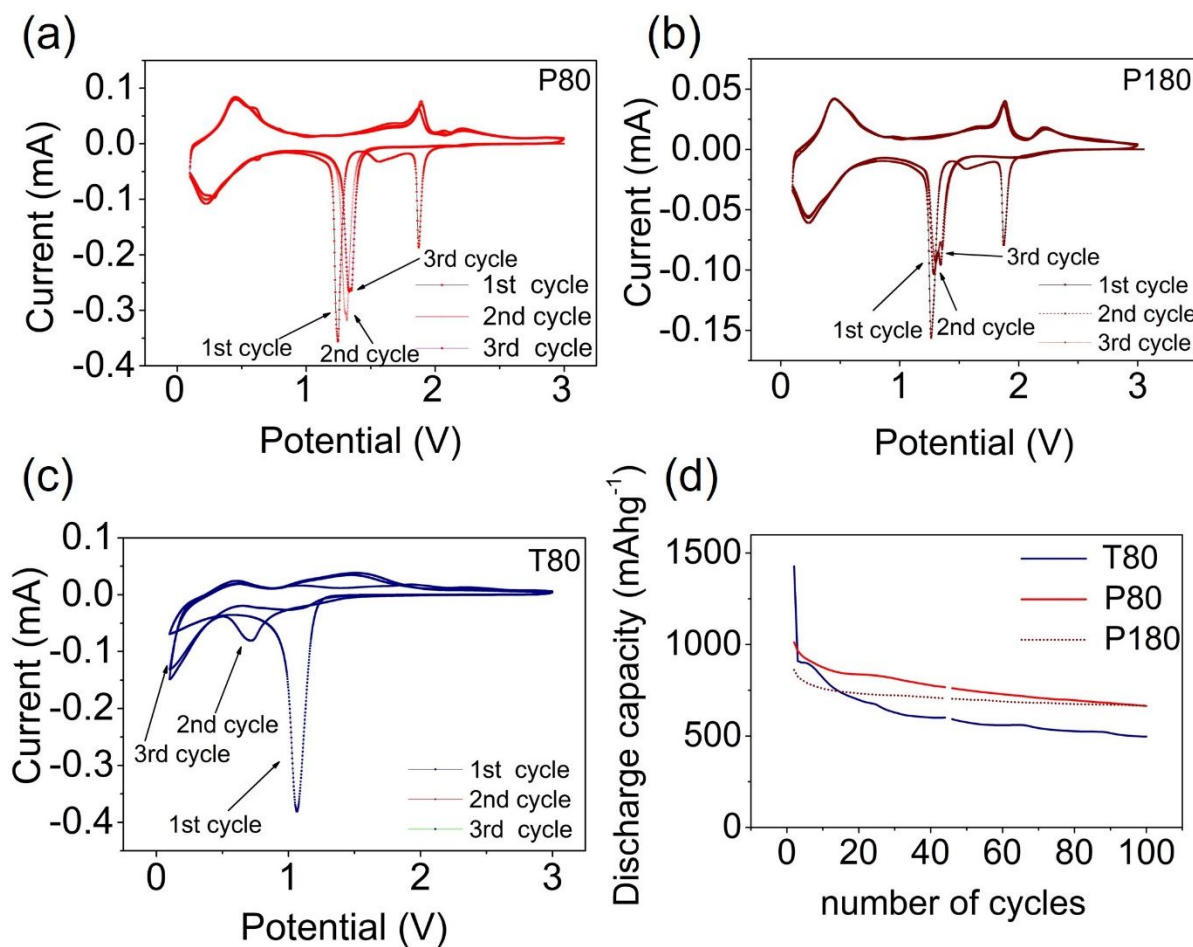


**Figure 6.** First three CV cycles at a scan rate of  $1 \text{ mV s}^{-1}$  of (a) P80 film, (b) P180 film, and (c) T80 film. (d) Discharge capacity of  $\text{SnS}_2$  films for 100 cycles at a current density of  $1 \text{ Ag}^{-1}$ .

The modification of the crystalline  $\text{SnS}_2$  anode has been further investigated by analyzing the crystallinity and elemental composition utilizing XRD and EDS techniques. After the cyclic voltammetry scans, the XRD analysis of the P180 film revealed an absence of characteristic peaks corresponding to the  $\text{SnS}_2$  phase. Instead, peaks corresponding to metallic tin appeared [Figure S8]. This transformation underscores the structural changes that occurred during the CV cycling. Complementary EDS analysis corroborated these findings, showing a substantial reduction in sulfur content within the films following CV scans [Figure S9]. Notably, the

presence of oxygen was detected in the films and can be attributed to air exposure afterwards the CV scans.

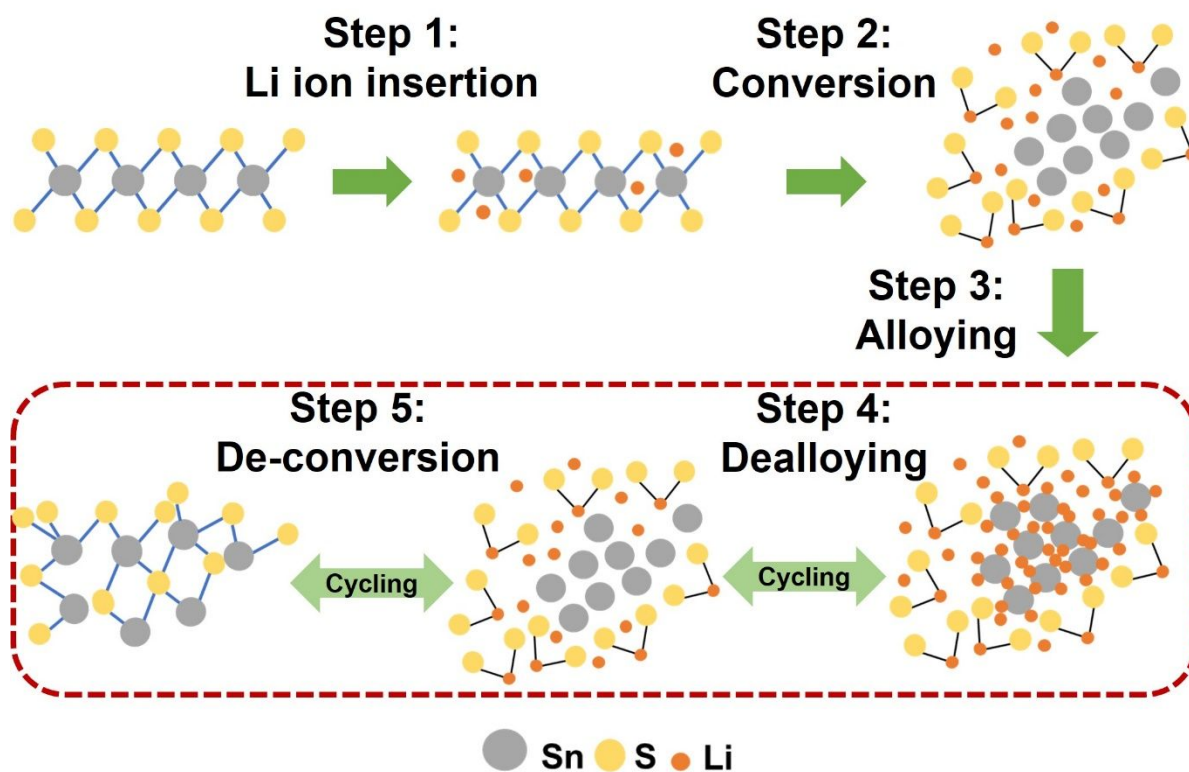


**Figure 7:** Representative schematic of the electrochemical reactions occurring at the crystalline SnS<sub>2</sub> anode material during the Li-ion battery cycling process.

On the contrary, during the first lithiation, the amorphous electrode does not exhibit any cathodic peaks corresponding to lithium intercalation. Instead, it shows cathodic peaks at 1.2 V and 0.1 V corresponding to the conversion and alloying reactions, respectively, similar to a previously reported amorphous SnS<sub>2</sub> electrode.<sup>58</sup> Except for the anodic peak at 0.4 V corresponding to the dealloying reaction, the delithiation process does not indicate the recovery of the SnS<sub>2</sub> structure. Upon further scanning, the electrode exhibits weak cathodic/anodic peaks corresponding to alloying/dealloying. According to a recent study, lithium intercalation into the crystal structure of SnS<sub>2</sub> prior to the conversion reaction leads to an even distribution of the

1  
2  
3  $\text{Li}_2\text{S}$  allowing a large portion of the active material to take part in the electrochemical  
4 reactions.<sup>59</sup> However, it is clear that the amorphous  $\text{SnS}_2$  does not exhibit lithium intercalation  
5 reactions. Also, it shows irreversible conversion reactions suggesting that the structure of the  
6 anode is altered and/or destroyed, preventing further  $\text{Li}^+$  ion insertion/extraction transport. The  
7 galvanostatic charge/discharge profile of all three electrodes is consistent with the  
8 corresponding CV profiles and is given in the supporting information [**Figure S10**].  
9

10  
11  
12  
13  
14  
15  
16  
17  
18 The cycling performance of the  $\text{SnS}_2$  electrodes was studied at a current density of  $1 \text{ Ag}^{-1}$  as  
19 shown in **Figure 6(d)**. The first discharge capacity of the amorphous electrode is  $1427 \text{ mAhg}^{-1}$   
20 <sup>1</sup> higher than the theoretical initial discharge capacity but fades rapidly with the number of  
21 cycles, and the final discharge capacity after 100 cycles is only  $496 \text{ mAhg}^{-1}$  exhibiting a non-  
22 ideal capacity retention of 34% after 100 charge/discharge cycles. This higher initial discharge  
23 capacity is likely due to the formation of a solid electrolyte interface.<sup>56</sup> Unlike the dramatic  
24 capacity fading displayed by the amorphous  $\text{SnS}_2$  electrode, the crystalline P80  $\text{SnS}_2$  electrode  
25 delivers a high initial capacity of  $1012 \text{ mAhg}^{-1}$ , which drops to  $664 \text{ mAhg}^{-1}$  at the 100<sup>th</sup> cycle.  
26  
27 This higher discharge capacity can be possibly due to the strong crystallite orientation of the  
28 film which is proven more favorable for the lithium intercalation/deintercalation reactions as  
29 per previous reports.<sup>60</sup> Retaining 65% of its initial capacity, the crystalline P80 electrode thus  
30 outperforms the amorphous T80 electrode. Even better cyclability is obtained for the crystalline  
31 P180  $\text{SnS}_2$  electrodes with OoPO structures. However, the P180 electrode shows a slightly  
32 lesser initial discharge capacity of  $861 \text{ mAhg}^{-1}$  which evolves to  $665 \text{ mAhg}^{-1}$  after 100 cycles  
33 thereby retaining 77% of the initial capacity. In this case, the capacity degrades more slowly  
34 and even becomes nearly steady after 80 charge/discharge cycles showing up as the best  
35 candidate in terms of capacity retention. Compared to many existing literature reports indicated  
36 in Table 2, the PE-ALD deposited  $\text{SnS}_2$  anodes demonstrate better cycling retention even after  
37 100 charge/discharge cycles. The P80 and P180 electrodes retain higher capacity (65% and  
38  
39  
40  
41  
42  
43  
44  
45  
46  
47  
48  
49  
50  
51  
52  
53  
54  
55  
56  
57  
58  
59  
60

77% respectively) compared to the SnS<sub>2</sub> nanosheets and carbonaceous polypyrrole nanotubes coated SnS<sub>2</sub> nanosheets (CPN@SnS<sub>2</sub>) (40% and 49%) reported by Chen et al.,<sup>61</sup> and SnS<sub>2</sub> nanoparticles and SnS<sub>2</sub>/SnO<sub>2</sub> nanoparticles (59% and 64%) tested by L. Yin et al.<sup>62</sup> but at lower initial capacity. Moreover, in comparison to the SnS<sub>2</sub> nanosheets reported by Kim et al.<sup>55</sup> which exhibit an initial discharge capacity of 300 mA h g<sup>-1</sup> and retain only 63% of the initial capacity after 50 cycles, the P80, P180 and T80 films show enhanced performance in terms of initial capacity as well as the capacity retention.

**Table 2.** Literature overview of the electrochemical performance of SnS<sub>2</sub> electrodes tested for Li-ion battery

Electrode	Specific capacity (mA h g <sup>-1</sup> )	Current density (A/g)	Cycle no	Retention (%)	Ref
CPN@SnS <sub>2</sub> nanosheets (coin cells)	1422	0.06	100	49	61
SnS <sub>2</sub> nanosheets (coin cells)	979.6	0.06	100	39	61
SnS <sub>2</sub> /SnO <sub>2</sub> composite NPs (coin cells)	1420.06	0.1	50	63	62
Plate-like SnS <sub>2</sub> NPs (coin cells)	1382.39	0.1	50	59	62
SnS <sub>2</sub> nanosheets (coin cells)	300	0.3	50	63	55
Amorphous SnS <sub>2</sub> -T80	1427	1	100	34	This work
Crystalline SnS <sub>2</sub> -P80	1012	1	100	65	This work
Crystalline SnS <sub>2</sub> -P180	861	1	100	77	This work

1  
2  
3 Hence, a clear influence of crystallinity can be observed on the discharge capacity and the  
4 cyclic performance of the SnS<sub>2</sub> electrodes. Compared to the amorphous film which  
5 demonstrates an irreversible conversion reaction of SnS<sub>2</sub> to Sn, crystalline films demonstrate  
6 partially reversible reactions along with improved cyclic performance clearly showing the  
7 predominance of crystallinity in enabling smooth and stable lithium insertion/extraction during  
8 prolonged cycling and hence improved capacity retention. Among the two crystalline  
9 electrodes, the SnS<sub>2</sub> electrode with OoPO structures exhibits steady cyclic performance despite  
10 its lower initial discharge capacity. Although the exact reason for the enhanced capacity  
11 retention is not fully understood, it is clear that the specific structural characteristics are  
12 beneficial for enhanced electrode stability and hence improved cyclic performance. An  
13 additional in-depth investigation is proposed to effectively understand structural correlations  
14 with electrochemical performance and can be applied to other layer metal dichalcogenide  
15 materials for better battery performance.

### 3.4 SnS<sub>2</sub> as the catalyst for electrochemical reduction of CO<sub>2</sub>

34  
35 All three SnS<sub>2</sub> films (~20 nm thickness) deposited on gas diffusion electrodes (GDE) were  
36 subjected to six-hour-long chronopotentiometry tests at 100 mA cm<sup>-2</sup> to assess their selectivity,  
37 activity, and stability [**Figure S11**]. The results offer an insight into the influence of the utilized  
38 ALD parameters on CO<sub>2</sub> electroreduction over SnS<sub>2</sub>-coated GDEs. **Figure 8(a)** depicts the  
39 Faradaic efficiency (FE) to formate of each of the SnS<sub>2</sub> thin films in which a clear distinction  
40 between the different samples can be observed. At the onset of the measurement, a clear  
41 disparity in terms of selectivity can be seen for P180, which only reached a selectivity of 64 ±  
42 2% at a current density of 100 mA cm<sup>-2</sup> whereas the other samples, P80 and T80, started around  
43 79 ± 5% and 80 ± 2%, respectively.

1  
2  
3 As observed, crystallinity is not the main factor governing the initial selectivity since both the  
4 crystalline (P80) and amorphous (T80) structures outperform the crystalline (P180) film. In  
5  
6  
7  
8 addition, XPS of the as-prepared films does not provide an immediate explanation for the  
9  
10  
11  
12 observed difference in formate FE, as  $\text{Sn}^{4+}$  was the only species detected in all three films  
13 [Figure S12 & Table S3]. However, after five minutes of chronopotentiometry at  $100 \text{ mA cm}^{-2}$ ,  
14  
15  
16  
17 XPS showed the presence of  $\text{Sn}^{2+}$  in all three films [Figure S13]. According to literature<sup>63</sup>,  
18  
19  
20  
21 the presence of  $\text{Sn}^{4+}$  effectively reduces the overpotential for the  $\text{CO}_2\text{RR}$ , while that of  $\text{Sn}^{2+}$  is  
22  
23  
24  
25 expected to enhance the selectivity to formate. Nevertheless, the share of  $\text{Sn}^{2+}$  was higher in  
26  
27  
28  
29  
30  
31  
32  
33  
34  
35  
36  
37  
38  
39  
40  
41  
42  
43  
44  
45  
46  
47  
48  
49  
50  
51  
52  
53  
54  
55  
56  
57  
58  
59  
60  
P80 relative to P180 and T80. Given the invariance in initial FE and overpotential between P80  
and T80, oxidation state does not seem to be the major descriptor of catalytic performance  
under these particular electrolyzer operating conditions.

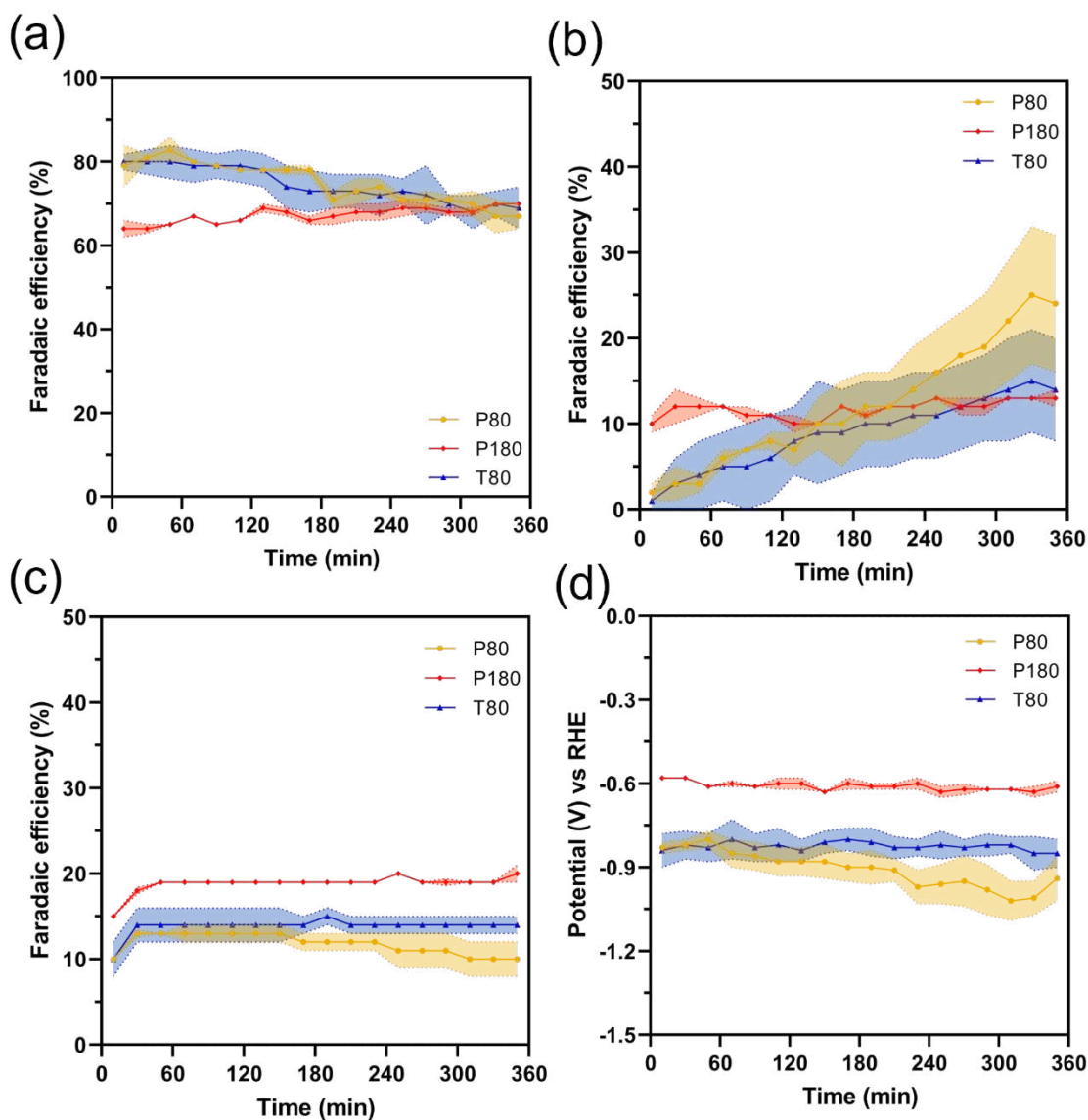


**Figure 8.** SnS<sub>2</sub> thin films deposited on a GDE used for the electrochemical CO<sub>2</sub> reduction tested in a flow-by reactor at 100 mA cm<sup>-2</sup> with 0.5 M KHCO<sub>3</sub> as catholyte and 2 M KOH as anolyte resulting in the following Faradaic efficiencies for (a) formate, (b) hydrogen, and (c) carbon monoxide while measuring the (d) potentials over six hours. The total FE amounted to 100 ± 4 % for all measurements.

It was, therefore, further hypothesized that the varying physical properties of the thin films, notably their roughness and hydrophobicity, could affect both the effective applied current

1  
2  
3 density (and thus overpotential) and the extent of electrolyte permeation into the catalyst  
4 layer<sup>64</sup>, which may thereby partially impede CO<sub>2</sub> mass transport. To test this hypothesis,  
5 contact angle (CA) measurements of as-prepared SnS<sub>2</sub>/GDEs and multiple control samples  
6 were performed. The surface of a bare GDE is hydrophobic mainly due to the incorporation of  
7 23 wt% of polytetrafluoroethylene (PTFE) in its microporous layer (MPL). This is manifested  
8 by a CA of 140.3 ± 0.3°. In contrast, the three SnS<sub>2</sub> thin films exhibited lower values. Firstly,  
9 the measured CAs of T80 and P80 were 126 ± 2°, and 90 ± 2°, respectively, thereby  
10 demonstrating the effect of the deposition technique on the hydrophobicity since both samples  
11 were prepared at 80 °C [Figure S14(c-f)]. P180, on the other hand, was significantly more  
12 hydrophilic, with a CA of 31 ± 1°.[Figure S14(g)]

13  
14  
15  
16  
17  
18  
19  
20  
21  
22  
23  
24  
25  
26  
27 The change in the films' hydrophobicity can be attributed to two factors: (i) lower apparent  
28 CA due to higher surface roughness (Wenzel state) and (ii) modification of the GDE surface.  
29 The latter effect arises from the highly reactive plasma environment to which the GDE was  
30 exposed, potentially leading to the functionalization of the carbon surface and/or  
31 redistribution/functionalization of PTFE in the MPL.<sup>65-66</sup> Additionally, the energetic species  
32 within the plasma may cause structural damage to the substrate through bombardment. Hence,  
33 to investigate the impact of plasma exposure on the hydrophobicity of the GDE, both its  
34 microporous layer (MPL) and gas diffusion layer (GDL) was evaluated for the influence of an  
35 H<sub>2</sub>S/Ar plasma in the absence of the Sn precursor. The hydrophobicity of the GDL - which  
36 contains only 5 wt% of PTFE - remained unaltered, as indicated by the comparable CA to its  
37 initial state (133.8 ± 0.3° for H<sub>2</sub>S/Ar plasma at 180 °C vs 137 ± 1° for the bare GDE)[Figure  
38 S15(b-f)]. However, a discernible change in hydrophobicity was observed in the MPL (107.3  
39 ± 0.5° for H<sub>2</sub>S/Ar plasma at 180 °C vs 140 ± 0.3° for the bare GDE) [Figure S15(a-e)]. This  
40 suggests that the modification induced by the plasma treatment primarily targeted the PTFE  
41 chains rather than the carbon structure. Furthermore, the Wenzel state describes a surface in  
42  
43  
44  
45  
46  
47  
48  
49  
50  
51  
52  
53  
54  
55  
56  
57  
58  
59  
60

1  
2  
3 which droplets penetrate easily due to increased roughness and strong adhesive forces.  $C_{dl}$   
4 measurements showed that the roughness was altered by depositing the SnS<sub>2</sub> films on the MPL  
5 of the GDE [Figure S16(a-e)]. Whereas the  $C_{dl}$  of a bare GDE equalled  $85 \pm 1 \mu\text{F cm}^{-2}$ , that of  
6 the SnS<sub>2</sub> films was lower due to the coverage of the substrate and the lower conductivity of  
7 SnS<sub>2</sub> relative to carbon. The  $C_{dl}$  increased from  $39 \pm 2 \mu\text{F cm}^{-2}$  for T80 to  $72 \pm 4 \mu\text{F cm}^{-2}$  for  
8 P80, thus providing a higher surface area for the same mass loading. A further increase in  
9 roughness and the highest  $C_{dl}$  of the series, i.e.  $82 \pm 3 \mu\text{F cm}^{-2}$ , was obtained with P180, in line  
10 with the lowest measured CA. Furthermore, cyclic voltammetry measurements of the initial  
11 SnS<sub>2</sub> thin films showed a reduction peak at -1.0 vs Ag/AgCl, which is attributed to SnS<sub>2</sub>  
12 reduction to metallic Sn with the release of S<sup>2-</sup> into solution<sup>67</sup> [Figure S17(a-d)]. Similarly, the  
13 reduction peak current increased with increasing roughness and decreasing CA. That  
14 correlation between the CA and the reduction peak current was proven to be significant and  
15 thus confirms the effect of roughness on the electrochemical activity of the SnS<sub>2</sub> thin films.  
16 Taken together, the difference in the initial selectivity and activity between the different SnS<sub>2</sub>  
17 samples is explained as follows: P180 has a rough surface with big out-of-plane structures  
18 while P80 and T80 have a smoother surface with smaller structures in comparison. Given that  
19 a rougher surface is typically correlated with a higher  $C_{dl}$  and thus a higher activity (for both  
20 CO<sub>2</sub>RR and the hydrogen evolution reaction), it is judged to be a major reason as to why P180  
21 has a lower overpotential ( $-0.580 \pm 0.003 \text{ V vs RHE}$ ) than P80 and T80 ( $-0.83 \pm 0.02 \text{ V}$  and -  
22  $0.84 \pm 0.06 \text{ V vs. RHE}$ , respectively).[Figure 8(d)]  
23  
24  
25  
26  
27  
28  
29  
30  
31  
32  
33  
34  
35  
36  
37  
38  
39  
40  
41  
42  
43  
44  
45  
46  
47  
48  
49  
50  
51  
52

53 When looking at the stability of those SnS<sub>2</sub> thin films, P180 clearly stands out [Fig. 8(a-c)]. It  
54 can be observed that the formate FE of P80 and T80 starts to decline - at the cost of increased  
55 hydrogen production - already after two hours of measurement. In contrast, P180 shows a  
56 slightly increasing formate FE trend, ultimately resulting in comparable values ( $70.3 \pm 0.2\%$ )  
57  
58  
59  
60

1  
2  
3 to P80 and T80 after 6 h. That change in performance is caused by the reduction of SnS<sub>2</sub> to Sn  
4 which brings down formate selectivity to about 70%<sup>68-69</sup> and the accompanying change in Sn  
5 morphology and film roughness. That change in morphology is visualized in **Figure 9(a-d)** for  
6 P80 and P180 [See **Figure S18** for T80 along with bare GDE] using SEM images taken before  
7 and after CO<sub>2</sub>RR. At the same time, SnS<sub>2</sub> reduction is confirmed by the elimination of the  
8 sulfur signal from the corresponding EDS data after CO<sub>2</sub>RR, as seen in **Figure 9(e)**.  
9  
10 Importantly, P180 still showed a fair coverage of the carbon substrate – a major reason for its  
11 steady potential and formate production. For P80 and T80, an apparent decrease in the carbon  
12 coverage of the film due to film reconstruction and particle formation is observed.  
13  
14 Consequently, the pores in the carbon substrate become more accessible to electrolyte and  
15 susceptible to electrolyte salt precipitation, as detected by the pronounced potassium signal  
16 intensity in the EDS spectra of **Figure 9(e)**. This in turn can result in elevated hydrogen  
17 production and lower formate FE since the carbon support also acts as a catalyst under such  
18 conditions.  
19  
20  
21  
22  
23  
24  
25  
26  
27  
28  
29  
30  
31  
32  
33  
34  
35

36 Finally, it is important to briefly discuss the differences in the measured C<sub>dl</sub> values before and  
37 after CO<sub>2</sub>RR [**Figure S19** and **Table S4**] and explain how they relate to the foregoing  
38 observations. As mentioned, the C<sub>dl</sub> before CO<sub>2</sub>RR did not exceed 85 μF cm<sup>-2</sup>. After 1 hr of  
39 CO<sub>2</sub>RR at 100 mA cm<sup>-2</sup>, a notable two orders of magnitude increase in C<sub>dl</sub> is recorded for all  
40 films, including a blank benchmark GDE. That increase comes as a consequence of  
41 electrowetting during chronopotentiometry and the induced changes in film morphology that  
42 lead to exposure of the carbon substrate. It is important to note that the C<sub>dl</sub> of P180 (3.7 mF  
43 cm<sup>-2</sup>) is roughly 15% lower in comparison to the other films, which we attribute to its more  
44 homogeneous coverage of the carbon substrate. These findings emphasize the importance of  
45 interfacial physical properties and restructuring of thin-film-based catalyst layers, and how  
46  
47  
48  
49  
50  
51  
52  
53  
54  
55  
56  
57  
58  
59  
60

seemingly minor variations in  $C_{dl}$  and CA can help rationalize their electrocatalytic performance and stability.

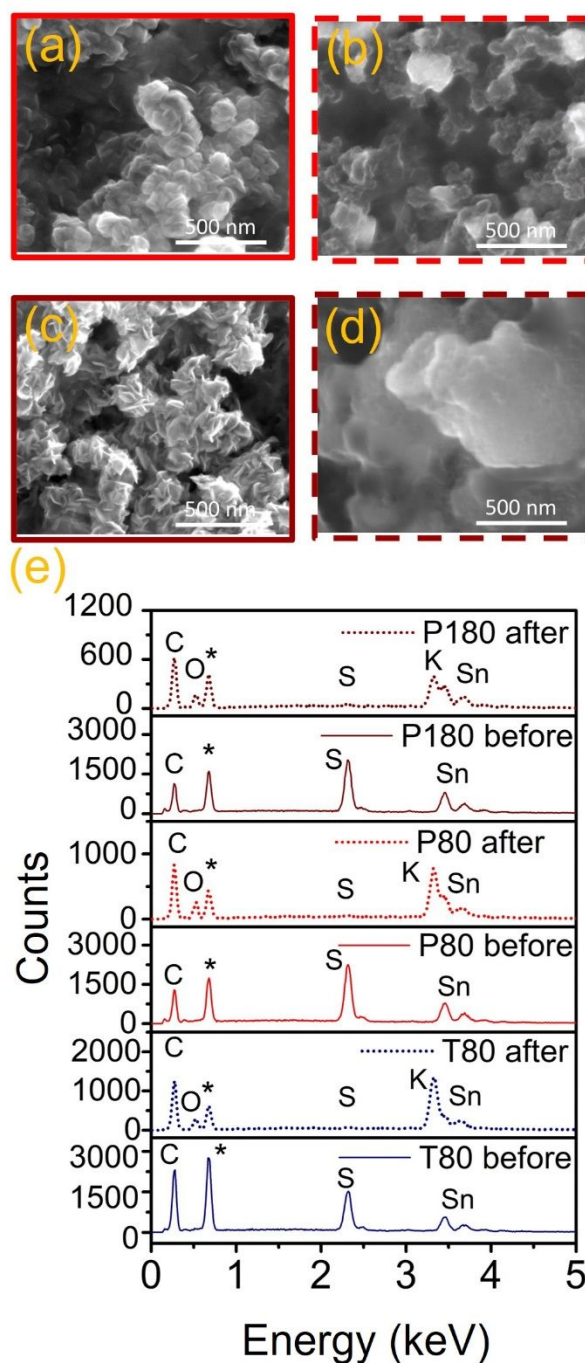


**Figure 9.** SEM image of SnS<sub>2</sub> deposited on a GDE by PE-ALD process at 80 °C (a) before CO<sub>2</sub>RR, and (b) after CO<sub>2</sub>RR, SEM image of SnS<sub>2</sub> deposited on a GDE by PE-ALD process at

180 °C (c) before CO<sub>2</sub>RR, and (d) after CO<sub>2</sub>RR, and (e) SEM-EDS of all tested SnS<sub>2</sub> thin films deposited on a GDE before and after CO<sub>2</sub>RR.

In comparison to other SnS<sub>2</sub> catalysts available in the literature, the activity of SnS<sub>2</sub> thin films prepared with ALD is improved, especially in terms of the overpotential [Table 3] For instance, P180 lowers the overpotential by 320 mV while the current density (more than eight-fold higher) and the FE (7% increase) exceed those of the SnS<sub>2</sub> nanosheets tested by Zhang *et al.*<sup>70</sup> P80 and T80 exhibit FEs that are reasonably comparable to those reported by Zhang *et al.* and Li *et al.* (87% and 84.5% respectively). However, the ALD-deposited SnS<sub>2</sub>/GDEs demonstrate superior activity, achieving both a higher current density at slightly higher overpotential.<sup>67, 70</sup> Moreover, this improved performance is obtained at extremely low catalyst loadings in comparison with typical literature reports. This further evidences the promising nature of thin films in general and SnS<sub>2</sub>-based thin films prepared by thermal ALD and PE-ALD in particular towards application in the CO<sub>2</sub>RR.

**Table 3.** Literature overview of SnS<sub>2</sub> electrocatalysts for CO<sub>2</sub>RR tested in the aqueous environment.

Catalyst	Loading	Catholyte	FE to formate	Current density (mA cm <sup>-2</sup> )	Potential	Ref.
SnS <sub>2</sub> NS H-cell	0.75 mg <sub>SnS<sub>2</sub></sub> cm <sup>-2</sup>	0.1 M KHCO <sub>3</sub>	57%	12.3	-0.9 V vs RHE	70
H-SnS <sub>2</sub> NS H-cell	0.75 mg <sub>H-SnS<sub>2</sub></sub> cm <sup>-2</sup>	0.1 M KHCO <sub>3</sub>	87%	18.6	-0.9 V vs RHE	70
SnS <sub>2</sub> /rGO Three electrode cell	0.0872 mg cm <sup>-2</sup>	0.5 M NaHCO <sub>3</sub>	84.5%	13.9	-1.4 V vs Ag/AgCl	67
Sn(S)/Au Three electrode cell	/	0.1 M KHCO <sub>3</sub>	93.3%	55	-0.75 vs RHE	25

Sn NPs/Au Three electrode cell	/	0.1 M KHCO <sub>3</sub>	30.2%	42	-0.75 vs RHE	25
SnS <sub>2</sub> P80	0.010 mg cm <sup>-2</sup>	0.5 M KHCO <sub>3</sub>	79%	100	-0.83 V vs RHE	This work
SnS <sub>2</sub> P180	0.008 mg cm <sup>-2</sup>	0.5 M KHCO <sub>3</sub>	64%	100	-0.58 V vs RHE	This work
SnS <sub>2</sub> T80	0.010 mg cm <sup>-2</sup>	0.5 M KHCO <sub>3</sub>	80%	100	-0.84 V vs RHE	This work

#### 4. CONCLUSION

This work succeeded in the PE-ALD of SnS<sub>2</sub> thin films using TDMASn precursor and H<sub>2</sub>S plasma. In contrast to the corresponding thermal ALD process, the PE-ALD process grows crystalline SnS<sub>2</sub> thin films at temperatures as low as 80 °C. XRD patterns confirmed the hexagonal crystal structure of SnS<sub>2</sub>. The presence of tin as Sn<sup>4+</sup> was also confirmed by XPS. SEM analysis revealed a continuous film surface consisting of small SnS<sub>2</sub> grains at 80°C, whereas the grains become larger at 180°C and eventually form out-of-plane oriented structures for larger film thicknesses. Optical transmission measurements indicated an indirect bandgap of 2.25 – 2.3 eV for the SnS<sub>2</sub> thin films.

Given the interest in SnS<sub>2</sub> for electrochemical energy conversion and storage applications, we compared the electrochemical performance of crystalline and amorphous SnS<sub>2</sub> thin films, deposited by PE-ALD and thermal ALD, respectively. Our results show that crystalline SnS<sub>2</sub> outperforms amorphous SnS<sub>2</sub> films in terms of cycle stability as anode material in lithium-ion batteries, with the best cycling performance established for thin films with out-of-plane oriented structures on their surface despite their lower initial capacity. The crystalline SnS<sub>2</sub> with out-of-plane orientation structures and grain-like structures and amorphous SnS<sub>2</sub> exhibit 77%, 65%, and 34% respectively of the capacity retention after 100 charge/discharge cycles. The CO<sub>2</sub> electroreduction results indicate the significant benefits of crystalline SnS<sub>2</sub> with out-

1  
2  
3 of-plane orientation structures as they result in a lower potential (-0.58 V vs RHE) but still  
4 provide decent and stable Faradaic efficiencies towards formate of 64% On the other hand, the  
5 amorphous SnS<sub>2</sub> and crystalline SnS<sub>2</sub> with small crystallite structures, improve the selectivity  
6 towards formate up to 80% at the cost of a higher potential (-0.83 V vs RHE) and significantly  
7 lower stability of the thin films. Therefore, it is evident that exploring the PE-ALD process  
8 offers a great opportunity to develop crystalline SnS<sub>2</sub> thin films at mild deposition temperatures  
9 and enables tuning of material properties suitable for various practical applications.  
10  
11  
12  
13  
14  
15  
16  
17  
18  
19

## 20 ASSOCIATED CONTENT

### 21 22 **Supporting Information**

23  
24  
25  
26 Calibration curve used for calculating the thickness of rough SnS<sub>2</sub> thin films, saturation curves  
27 of the PE-ALD process at 180 °C and thermal ALD process at 80 °C and 180 °C, XRD pattern  
28 of SnS<sub>x</sub> films deposited by thermal ALD in high resolution, XPS survey spectra of SnS<sub>x</sub> films  
29 on the surface and after the 20 s of argon sputtering, table with atomic concentration of all  
30 elements detected on the surface of SnS<sub>x</sub> films, transmittance spectra and tauc plot of PE-ALD  
31 deposited SnS<sub>2</sub> films, SEM images of SnS<sub>2</sub> films deposited on TiN substrate, Sn 3d and S 2p  
32 XPS spectra of SnS<sub>2</sub> deposited on TiN substrate, table with binding energies of Sn 3d<sub>5/2</sub> and S  
33 2p<sub>3/2</sub> spectra and atomic concentration of all elements detected on the surface of SnS<sub>2</sub> films  
34 deposited on TiN substrate, charge/discharge voltage profile of SnS<sub>2</sub> thin films in Li-ion  
35 battery testing, the chronopotentiometry measurements of SnS<sub>2</sub> thin films for CO<sub>2</sub>RR, Sn 3d  
36 and S 2p XPS spectra of SnS<sub>2</sub> films deposited on GDE, table with binding energies of Sn 3d<sub>5/2</sub>  
37 and S 2p<sub>3/2</sub> spectra and atomic concentration of all elements detected on the surface of SnS<sub>2</sub>  
38 films deposited on GDE, Sn 3d XPS spectra of SnS<sub>2</sub> films deposited on GDE after  
39 chronopotentiometry measurements, the contact angles of bare Sigracet 39BB GDE and SnS<sub>2</sub>  
40 deposited GDE, the contact angles of bare Sigracet 39BB GDE and SnS<sub>2</sub> deposited GDE  
41  
42  
43  
44  
45  
46  
47  
48  
49  
50  
51  
52  
53  
54  
55  
56  
57  
58  
59  
60

1  
2  
3 exposed to H<sub>2</sub>/Ar plasma, SEM image of bare GDE and SnS<sub>2</sub> deposited by thermal ALD  
4  
5 process at 80 °C before and after CO<sub>2</sub> electroreduction, the electrochemical active surface area  
6  
7 of the unused bare GDE and SnS<sub>2</sub> deposited GDE calculated from the cyclic voltammetry  
8  
9 measurements, the cyclic voltammetry measurements of before and after chronopotentiometry  
10  
11 measurements, the electrochemical active surface area of the used bare GDE and SnS<sub>2</sub>  
12  
13 deposited GDE calculated from the cyclic voltammetry measurements, and table with the  
14  
15 EASA of the SnS<sub>2</sub> thin films before and after CO<sub>2</sub>RR.  
16  
17  
18  
19  
20  
21  
22

## 23 AUTHOR INFORMATION

### 24 **Corresponding Author**

25  
26 \*Email: Jolien.Dendooven@Ugent.be  
27

### 28 **Author Contributions**

29  
30 The manuscript was written with contributions from all authors. All authors approved the final  
31  
32 version of the manuscript.  
33  
34  
35  
36  
37  
38

### 39 **Acknowledgements**

40  
41 This work has received funding from the Special Research Fund BOF of Ghent University  
42  
43 (GOA-01G01019). Part of this research is conducted within the project entitled SYN-CAT  
44  
45 (HBC.2020.2614) funded by VLAIO (Flanders Innovation & Entrepreneurship) under  
46  
47 the Flanders Industry Innovation Moonshot programme. We would like to thank Jin Li and  
48  
49 Matthias Minjauw for the XPS measurements and Olivier Janssens for the SEM-EDS  
50  
51 measurements. Ranjith K Ramachandran and Davy Deduytsche are acknowledged for guiding  
52  
53 the maintenance of the ALD reactor. Finally, we would like to thank Henk Vrielinck and  
54  
55 Samira Khelifi for assisting with the analysis of optical properties and Véronique Cremers and  
56  
57 Lowie Henderick for providing suggestions for writing the manuscript. .  
58  
59  
60

## REFERENCES

1. Lee, S.; Shin, S.; Ham, G.; Lee, J.; Choi, H.; Park, H.; Jeon, H., Characteristics of Layered Tin Disulfide Deposited by Atomic Layer Deposition with H<sub>2</sub>s Annealing. *AIP Adv.* **2017**, *7* (4), 045307.
2. Voiry, D.; Yang, J.; Chhowalla, M., Recent Strategies for Improving the Catalytic Activity of 2d TMD Nanosheets toward the Hydrogen Evolution Reaction. *Adv. Mater.* **2016**, *28* (29), 6197-6206.
3. Asadi, M.; Kim, K.; Liu, C.; Addepalli, A. V.; Abbasi, P.; Yasaei, P.; Phillips, P.; Behranginia, A.; Cerrato, J. M.; Haasch, R., Nanostructured Transition Metal Dichalcogenide Electrocatalysts for CO<sub>2</sub> Reduction in Ionic Liquid. *Science* **2016**, *353* (6298), 467-470.
4. Cao, X.; Tan, C.; Zhang, X.; Zhao, W.; Zhang, H., Solution-Processed Two-Dimensional Metal Dichalcogenide-Based Nanomaterials for Energy Storage and Conversion. *Adv. Mater.* **2016**, *28* (29), 6167-6196.
5. Leng, K.; Chen, Z.; Zhao, X.; Tang, W.; Tian, B.; Nai, C. T.; Zhou, W.; Loh, K. P., Phase Restructuring in Transition Metal Dichalcogenides for Highly Stable Energy Storage. *ACS nano* **2016**, *10* (10), 9208-9215.
6. Radisavljevic, B.; Radenovic, A.; Brivio, J.; Giacometti, V.; Kis, A., Single-Layer MoS<sub>2</sub> Transistors. *Nat. Nanotechnol.* **2011**, *6* (3), 147-150.
7. Chhowalla, M.; Jena, D.; Zhang, H., Two-Dimensional Semiconductors for Transistors. *Nat. Rev. Mater.* **2016**, *1* (11), 1-15.
8. Somvanshi, D.; Jit, S., Transition Metal Dichalcogenides Based Two-Dimensional Heterostructures for Optoelectronic Applications. In *2d Nanoscale Heterostructured Materials*, Elsevier: 2020; pp 125-149.
9. Thakar, K.; Lodha, S., Optoelectronic and Photonic Devices Based on Transition Metal Dichalcogenides. *Mater. Res. Express* **2020**, *7* (1), 014002.
10. Tan, C.; Lai, Z.; Zhang, H., Ultrathin Two-Dimensional Multinary Layered Metal Chalcogenide Nanomaterials. *Adv. Mater.* **2017**, *29* (37), 1701392.
11. Hu, Y.; Huang, Y.; Tan, C.; Zhang, X.; Lu, Q.; Sindoro, M.; Huang, X.; Huang, W.; Wang, L.; Zhang, H., Two-Dimensional Transition Metal Dichalcogenide Nanomaterials for Biosensing Applications. *Mater. Chem. Front.* **2017**, *1* (1), 24-36.
12. Kannan, P. K.; Late, D. J.; Morgan, H.; Rout, C. S., Recent Developments in 2D Layered Inorganic Nanomaterials for Sensing. *Nanoscale* **2015**, *7* (32), 13293-13312.
13. Choi, H.; Lee, J.; Shin, S.; Lee, J.; Lee, S.; Park, H.; Kwon, S.; Lee, N.; Bang, M.; Lee, S.-B., Fabrication of High Crystalline SnS and SnS<sub>2</sub> Thin Films, and Their Switching Device Characteristics. *Nanotechnology* **2018**, *29* (21), 215201.
14. Burton, L. A.; Whittles, T. J.; Hesp, D.; Linhart, W. M.; Skelton, J. M.; Hou, B.; Webster, R. F.; O'Dowd, G.; Reece, C.; Cherns, D., Electronic and Optical Properties of Single Crystal SnS<sub>2</sub>: An Earth-Abundant Disulfide Photocatalyst. *J. Mater. Chem. A* **2016**, *4* (4), 1312-1318.
15. Su, G.; Hadjiev, V. G.; Loya, P. E.; Zhang, J.; Lei, S.; Maharjan, S.; Dong, P.; M. Ajayan, P.; Lou, J.; Peng, H., Chemical Vapor Deposition of Thin Crystals of Layered Semiconductor SnS<sub>2</sub> for Fast Photodetection Application. *Nano Lett.* **2015**, *15* (1), 506-513.
16. Suzuki, K.; Chantana, J.; Minemoto, T., Na Role During Sulfurization of NaF/Cu/SnS<sub>2</sub> Stacked Precursor for Formation of Cu<sub>2</sub>SnS<sub>3</sub> Thin Film as Absorber of Solar Cell. *Appl. Surf. Sci.* **2017**, *414*, 140-146.
17. Yu, J.; Xu, C.-Y.; Ma, F.-X.; Hu, S.-P.; Zhang, Y.-W.; Zhen, L., Monodisperse SnS<sub>2</sub> Nanosheets for High-Performance Photocatalytic Hydrogen Generation. *ACS Appl. Mater. Interfaces* **2014**, *6* (24), 22370-22377.
18. Gao, Y.; Bai, L.; Zhang, X.; Yang, F., Non-Parallel Photo-Assisted Electrocatalysis Mechanism of SnS<sub>2</sub>/NiO Heterojunction for Efficient Electrocatalytic Oxygen Evolution Reaction. *ChemElectroChem* **2021**, *8* (11), 2087-2093.

- 1  
2  
3  
4  
5  
6  
7  
8  
9  
10  
11  
12  
13  
14  
15  
16  
17  
18  
19  
20  
21  
22  
23  
24  
25  
26  
27  
28  
29  
30  
31  
32  
33  
34  
35  
36  
37  
38  
39  
40  
41  
42  
43  
44  
45  
46  
47  
48  
49  
50  
51  
52  
53  
54  
55  
56  
57  
58  
59  
60
19. Sun, Y.; Cheng, H.; Gao, S.; Sun, Z.; Liu, Q.; Liu, Q.; Lei, F.; Yao, T.; He, J.; Wei, S., Freestanding Tin Disulfide Single-Layers Realizing Efficient Visible-Light Water Splitting. *Angew. Chem., Int. Ed.* **2012**, *51* (35), 8727-8731.
  20. Seo, J. w.; Jang, J. t.; Park, S. w.; Kim, C.; Park, B.; Cheon, J., Two-Dimensional SnS<sub>2</sub> Nanoplates with Extraordinary High Discharge Capacity for Lithium Ion Batteries. *Adv. Mater.* **2008**, *20* (22), 4269-4273.
  21. He, J.; Liu, X.; Liu, H.; Zhao, Z.; Ding, Y.; Luo, J., Highly Selective Electrocatalytic Reduction of CO<sub>2</sub> to Formate over Tin (IV) Sulfide Monolayers. *J. Catal.* **2018**, *364*, 125-130.
  22. Huang, Z. X.; Wang, Y.; Liu, B.; Kong, D.; Zhang, J.; Chen, T.; Yang, H. Y., Unlocking the Potential of SnS<sub>2</sub>: Transition Metal Catalyzed Utilization of Reversible Conversion and Alloying Reactions. *Sci. Rep.* **2017**, *7* (1), 1-11.
  23. Xu, X.; Liu, W.; Kim, Y.; Cho, J., Nanostructured Transition Metal Sulfides for Lithium Ion Batteries: Progress and Challenges. *Nano Today* **2014**, *9* (5), 604-630.
  24. Zhai, C.; Du, N.; Yang, H. Z. D., Large-Scale Synthesis of Ultrathin Hexagonal Tin Disulfide Nanosheets with Highly Reversible Lithium Storage. *Chem. Commun.* **2011**, *47* (4), 1270-1272.
  25. Zheng, X.; De Luna, P.; de Arquer, F. P. G.; Zhang, B.; Becknell, N.; Ross, M. B.; Li, Y.; Banis, M. N.; Li, Y.; Liu, M., Sulfur-Modulated Tin Sites Enable Highly Selective Electrochemical Reduction of CO<sub>2</sub> to Formate. *Joule* **2017**, *1* (4), 794-805.
  26. Shao, X.; Zhang, X.; Liu, Y.; Qiao, J.; Zhou, X.-D.; Xu, N.; Malcombe, J. L.; Yi, J.; Zhang, J., Metal Chalcogenide-Associated Catalysts Enabling CO<sub>2</sub> Electroreduction to Produce Low-Carbon Fuels for Energy Storage and Emission Reduction: Catalyst Structure, Morphology, Performance, and Mechanism. *J. Mater. Chem. A* **2021**, *9* (5), 2526-2559.
  27. Chi, D.; Yang, H.; Du, Y.; Lv, T.; Sui, G.; Wang, H.; Lu, J., Morphology-Controlled CuO Nanoparticles for Electroreduction of CO<sub>2</sub> to Ethanol. *RSC Adv.* **2014**, *4* (70), 37329-37332.
  28. Zhao, S.; Li, S.; Guo, T.; Zhang, S.; Wang, J.; Wu, Y.; Chen, Y., Advances in Sn-Based Catalysts for Electrochemical CO<sub>2</sub> Reduction. *Nano-Micro Lett.* **2019**, *11* (1), 1-19.
  29. Johnson, R. W.; Hultqvist, A.; Bent, S. F., A Brief Review of Atomic Layer Deposition: From Fundamentals to Applications. *Mater. Today* **2014**, *17* (5), 236-246.
  30. George, S. M., Atomic Layer Deposition: An Overview. *Chem. Rev.* **2010**, *110* (1), 111-131.
  31. Pyeon, J. J.; Baek, I.-H.; Lee, W. C.; Lee, H.; Won, S. O.; Lee, G.-Y.; Chung, T.-M.; Han, J. H.; Baek, S.-H.; Kim, J.-S., Wafer-Scale, Conformal, and Low-Temperature Synthesis of Layered Tin Disulfides for Emerging Nonplanar and Flexible Electronics. *ACS Appl. Mater. Interfaces* **2019**, *12* (2), 2679-2686.
  32. Mattinen, M.; King, P. J.; Khriachtchev, L.; Meinander, K.; Gibbon, J. T.; Dhanak, V. R.; Räisänen, J.; Ritala, M.; Leskelä, M., Low-Temperature Wafer-Scale Deposition of Continuous 2D SnS<sub>2</sub> Films. *Small* **2018**, *14* (21), 1800547.
  33. Thimsen, E.; Riha, S. C.; Baryshev, S. V.; Martinson, A. B.; Elam, J. W.; Pellin, M. J., Atomic Layer Deposition of the Quaternary Chalcogenide Cu<sub>2</sub>ZnSnS<sub>4</sub>. *Chem. Mater.* **2012**, *24* (16), 3188-3196.
  34. Elam, J. W.; Baker, D. A.; Hryn, A. J.; Martinson, A. B.; Pellin, M. J.; Hupp, J. T., Atomic Layer Deposition of Tin Oxide Films Using Tetrakis (Dimethylamino) Tin. *J. Vac. Sci. Technol., A* **2008**, *26* (2), 244-252.
  35. Ansari, M. Z.; Nandi, D. K.; Janicek, P.; Ansari, S. A.; Ramesh, R.; Cheon, T.; Shong, B.; Kim, S.-H., Low-Temperature Atomic Layer Deposition of Highly Conformal Tin Nitride Thin Films for Energy Storage Devices. *ACS Appl. Mater. Interfaces* **2019**, *11* (46), 43608-43621.
  36. Poonkottil, N.; Ramachandran, R. K.; Solano, E.; Srinath, N. V.; Feng, J.-Y.; Werbrouck, A.; Van Daele, M.; Filez, M.; Minjauw, M. M.; Poelman, H., Selective Vapor-Phase Doping of Pt Nanoparticles into Phase-Controlled Nanoalloys. *J. Phys. Chem. C* **2022**, *126* (3), 1426-1438.
  37. Ham, G.; Shin, S.; Park, J.; Choi, H.; Kim, J.; Lee, Y.-A.; Seo, H.; Jeon, H., Tuning the Electronic Structure of Tin Sulfides Grown by Atomic Layer Deposition. *ACS Appl. Mater. Interfaces* **2013**, *5* (18), 8889-8896.

- 1  
2  
3 38. Basuvalingam, S. B.; Zhang, Y.; Bloodgood, M. A.; Godiksen, R. H.; Curto, A. G.; Hofmann, J.  
4 P.; Verheijen, M. A.; Kessels, W. M.; Bol, A. A., Low-Temperature Phase-Controlled Synthesis of  
5 Titanium Di- and Tri-Sulfide by Atomic Layer Deposition. *Chem. Mater.* **2019**, *31* (22), 9354-9362.
- 6 39. Mattinen, M.; Gity, F.; Coleman, E.; Vonk, J. F.; Verheijen, M. A.; Duffy, R.; Kessels, W. M.;  
7 Bol, A. A., Atomic Layer Deposition of Large-Area Polycrystalline Transition Metal Dichalcogenides  
8 from 100° C through Control of Plasma Chemistry. *Chem. Mater.* **2022**, *34* (16), 7280-7292.
- 9 40. Mathew, F.; Poonkottil, N.; Solano, E.; Poelman, D.; Hens, Z.; Detavernier, C.; Dendooven, J.,  
10 Plasma-Enhanced Atomic Layer Deposition of Crystalline Ga<sub>2</sub>S<sub>3</sub> Thin Films. *J. Vac. Sci. Technol., A*  
11 **2023**, *41* (6).
- 12 41. Dasgupta, N. P.; Mack, J. F.; Langston, M. C.; Bousetta, A.; Prinz, F. B., Design of an Atomic  
13 Layer Deposition Reactor for Hydrogen Sulfide Compatibility. *Rev. Sci. Instrum.* **2010**, *81* (4), 044102.
- 14 42. Dobbelaere, T.; Vereecken, P. M.; Detavernier, C., A Usb-Controlled  
15 Potentiostat/Galvanostat for Thin-Film Battery Characterization. *HardwareX* **2017**, *2*, 34-49.
- 16 43. Kim, S. B.; Zhao, X.; Davis, L. M.; Jayaraman, A.; Yang, C.; Gordon, R. G., Atomic Layer  
17 Deposition of Tin Monosulfide Using Vapor from Liquid Bis (N, N'-Diisopropylformamidinato) Tin (II)  
18 and H<sub>2</sub>s. *ACS Appl. Mater. Interfaces* **2019**, *11* (49), 45892-45902.
- 19 44. Meng, X.; Libera, J. A.; Fister, T. T.; Zhou, H.; Hedlund, J. K.; Fenter, P.; Elam, J. W., Atomic  
20 Layer Deposition of Gallium Sulfide Films Using Hexakis (Dimethylamido) Digallium and Hydrogen  
21 Sulfide. *Chem. Mater.* **2014**, *26* (2), 1029-1039.
- 22 45. Dasgupta, N. P.; Meng, X.; Elam, J. W.; Martinson, A. B., Atomic Layer Deposition of Metal  
23 Sulfide Materials. *Acc. Chem. Res.* **2015**, *48* (2), 341-348.
- 24 46. Mullings, M. N.; Hägglund, C.; Bent, S. F., Tin Oxide Atomic Layer Deposition from Tetrakis  
25 (Dimethylamino) Tin and Water. *J. Vac. Sci. Technol., A* **2013**, *31* (6).
- 26 47. Sharma, A.; Verheijen, M. A.; Wu, L.; Karwal, S.; Vandalon, V.; Knoops, H. C.; Sundaram, R. S.;  
27 Hofmann, J. P.; Kessels, W. E.; Bol, A. A., Low-Temperature Plasma-Enhanced Atomic Layer  
28 Deposition of 2-D MoS<sub>2</sub>: Large Area, Thickness Control and Tuneable Morphology. *Nanoscale* **2018**,  
29 *10* (18), 8615-8627.
- 30 48. Huang, C.-C.; Lin, Y.-J.; Chuang, C.-Y.; Liu, C.-J.; Yang, Y.-W., Conduction-Type Control of SnSx  
31 Films Prepared by the Sol-Gel Method for Different Sulfur Contents. *J. Alloys Compd.* **2013**, *553*, 208-  
32 211.
- 33 49. Whittles, T. J.; Burton, L. A.; Skelton, J. M.; Walsh, A.; Veal, T. D.; Dhanak, V. R., Band  
34 Alignments, Valence Bands, and Core Levels in the Tin Sulfides SnS, SnS<sub>2</sub>, and Sn<sub>2</sub>S<sub>3</sub>: Experiment and  
35 Theory. *Chem. Mater.* **2016**, *28* (11), 3718-3726.
- 36 50. Bugot, C.; Bouttemy, M.; Schneider, N.; Etcheberry, A.; Lincot, D.; Donsanti, F., New Insights  
37 on the Chemistry of Plasma-Enhanced Atomic Layer Deposition of Indium Oxysulfide Thin Films and  
38 Their Use as Buffer Layers in Cu (In, Ga) Se<sub>2</sub> Thin Film Solar Cell. *J. Vac. Sci. Technol., A* **2018**, *36* (6).
- 39 51. Burton, L. A.; Colombara, D.; Abellon, R. D.; Grozema, F. C.; Peter, L. M.; Savenije, T. J.;  
40 Dennler, G.; Walsh, A., Synthesis, Characterization, and Electronic Structure of Single-Crystal SnS,  
41 Sn<sub>2</sub>S<sub>3</sub>, and SnS<sub>2</sub>. *Chem. Mater.* **2013**, *25* (24), 4908-4916.
- 42 52. George, J.; Joseph, K., Absorption Edge Measurements in Tin Disulphide Thin Films. *J. Phys.*  
43 *D: Appl. Phys.* **1982**, *15* (6), 1109.
- 44 53. Jiang, Y.; Song, D.; Wu, J.; Wang, Z.; Huang, S.; Xu, Y.; Chen, Z.; Zhao, B.; Zhang, J., Sandwich-  
45 Like SnS<sub>2</sub>/Graphene/SnS<sub>2</sub> with Expanded Interlayer Distance as High-Rate Lithium/Sodium-Ion  
46 Battery Anode Materials. *ACS nano* **2019**, *13* (8), 9100-9111.
- 47 54. Xie, R.; Cui, Y.; Zhou, T.; Ren, J.; Zhuo, L.; Luo, J.; Li, C.; Liu, X., Unveiling the Structural  
48 Evolution of 1T SnS<sub>2</sub> Anode Upon Lithiation/Delithiation by Tem. *Chem. Commun.* **2019**, *55* (54),  
49 7800-7803.
- 50 55. Kim, T.-J.; Kim, C.; Son, D.; Choi, M.; Park, B., Novel SnS<sub>2</sub>-Nanosheet Anodes for Lithium-Ion  
51 Batteries. *J. Power Sources* **2007**, *167* (2), 529-535.
- 52 56. Wang, L.; Zhuo, L.; Yu, Y.; Zhao, F., High-Rate Performance of SnS<sub>2</sub> Nanoplates without  
53 Carbon-Coating as Anode Material for Lithium Ion Batteries. *Electrochim. Acta* **2013**, *112*, 439-447.
- 54  
55  
56  
57  
58  
59  
60

- 1  
2  
3 57. Bhaskar, A.; Deepa, M.; Rao, T. N., Tin Disulfide Nanoflowers Versus Nanosheets as Anodes  
4 in Lithium-Ion Batteries: How the Nanostructure Controls Performance. *Electrochim. Acta* **2015**, *184*,  
5 239-249.
- 6 58. Momma, T.; Shiraishi, N.; Yoshizawa, A.; Osaka, T.; Gedanken, A.; Zhu, J.; Sominski, L., SnS<sub>2</sub>  
7 Anode for Rechargeable Lithium Battery. *J. Power Sources* **2001**, *97*, 198-200.
- 8 59. Glibo, A.; Eshraghi, N.; Surace, Y.; Mautner, A.; Flandorfer, H.; Cupid, D. M., Comparative  
9 Study of Electrochemical Properties of SnS and SnS<sub>2</sub> as Anode Materials in Lithium-Ion Batteries.  
10 *Electrochim. Acta* **2023**, *441*, 141725.
- 11 60. Liu, S.; Lu, X.; Xie, J.; Cao, G.; Zhu, T.; Zhao, X., Preferential C-Axis Orientation of Ultrathin  
12 SnS<sub>2</sub> Nanoplates on Graphene as High-Performance Anode for Li-Ion Batteries. *ACS Appl. Mater.*  
13 *Interfaces* **2013**, *5* (5), 1588-1595.
- 14 61. Chen, X.; Huang, Y.; Zhang, K.; Feng, X.; Wang, M., Synthesis and High-Performance of  
15 Carbonaceous Polypyrrole Nanotubes Coated with SnS<sub>2</sub> Nanosheets Anode Materials for Lithium Ion  
16 Batteries. *Chem. Eng. J.* **2017**, *330*, 470-479.
- 17 62. Yin, L.; Chai, S.; Huang, J.; Kong, X.; Pan, L., Preparation of Hierarchical SnS<sub>2</sub>/SnO<sub>2</sub> Anode  
18 with Enhanced Electrochemical Performances for Lithium-Ion Battery. *Electrochim. Acta* **2017**, *238*,  
19 168-177.
- 20 63. An, X.; Li, S.; Yoshida, A.; Wang, Z.; Hao, X.; Abudula, A.; Guan, G., Electrodeposition of Tin-  
21 Based Electrocatalysts with Different Surface Tin Species Distributions for Electrochemical Reduction  
22 of CO<sub>2</sub> to HCOOH. *ACS Sustainable Chem. Eng.* **2019**, *7* (10), 9360-9368.
- 23 64. De Mot, B.; Hereijgers, J.; Duarte, M.; Breugelmans, T., Influence of Flow and Pressure  
24 Distribution inside a Gas Diffusion Electrode on the Performance of a Flow-by CO<sub>2</sub> Electrolyzer.  
25 *Chem. Eng. J.* **2019**, *378*, 122224.
- 26 65. Okuyama, H.; Kanamoto, T.; Porter, R., Solid-State Deformation of Polytetrafluoroethylene  
27 Powder: Part I Extrusion Drawing. *J. Mater. Sci.* **1994**, *29*, 6485-6494.
- 28 66. Roy, A. K.; Dendooven, J.; Deduytsche, D.; Devloo-Casier, K.; Ragaert, K.; Cardon, L.;  
29 Detavernier, C., Plasma-Enhanced Atomic Layer Deposition: A Gas-Phase Route to Hydrophilic,  
30 Glueable Polytetrafluoroethylene. *Chem. Commun.* **2015**, *51* (17), 3556-3558.
- 31 67. Li, F.; Chen, L.; Xue, M.; Williams, T.; Zhang, Y.; MacFarlane, D. R.; Zhang, J., Towards a Better  
32 Sn: Efficient Electrocatalytic Reduction of CO<sub>2</sub> to Formate by Sn/SnS<sub>2</sub> Derived from SnS<sub>2</sub>  
33 Nanosheets. *Nano Energy* **2017**, *31*, 270-277.
- 34 68. Van Daele, K.; De Mot, B.; Pupo, M.; Daems, N.; Pant, D.; Kortlever, R.; Breugelmans, T., Sn-  
35 Based Electrocatalyst Stability: A Crucial Piece to the Puzzle for the Electrochemical CO<sub>2</sub> Reduction  
36 toward Formic Acid. *ACS Energy Lett.* **2021**, *6* (12), 4317-4327.
- 37 69. Del Castillo, A.; Alvarez-Guerra, M.; Solla-Gullón, J.; Sáez, A.; Montiel, V.; Irabien, A., Sn  
38 Nanoparticles on Gas Diffusion Electrodes: Synthesis, Characterization and Use for Continuous CO<sub>2</sub>  
39 Electroreduction to Formate. *J. CO<sub>2</sub> Util.* **2017**, *18*, 222-228.
- 40 70. Zhang, A.; Liang, Y.; Li, H.; Wang, S.; Chang, Q.; Peng, K.; Geng, Z.; Zeng, J., Electronic Tuning  
41 of SnS<sub>2</sub> Nanosheets by Hydrogen Incorporation for Efficient CO<sub>2</sub> Electroreduction. *Nano Lett.* **2021**,  
42 *21* (18), 7789-7795.
- 43  
44  
45  
46  
47  
48  
49  
50  
51  
52  
53  
54  
55  
56  
57  
58  
59  
60

TABLE OF CONTENTS

